REVIEWS OF TOPICAL PROBLEMS

PACS numbers: **51.50.+v**, **52.80.–s**, **52.90.+z**

Optical discharge in the field of a Bessel laser beam

L N Pyatnitskii

DOI: 10.3367/UFNe.0180.201002c.0165

Contents

Abstract. The propagation features of laser radiation are discussed for the case of axiconic focusing. Issues explored include the nature of gas breakdown in the field of a Bessel laser beam, the gasdynamic expansion of the breakdown plasma, and how optical discharges and plasma channels are structured.

1. Introduction

Optical discharge, which was discovered in the focusing of laser radiation [1] in 1962, immediately attracted the attention of researchers. Subsequently, the new phenomenon was explained in numerous papers (e.g., Refs [2–7]), including even an article in *Fizicheskaya Entsiklopediya* (Encyclopedia of Physics) (1992). To produce an optical discharge, laser radiation was focused with a spherical lens. As is well known, a Gaussian wave beam with a plane wave front forms in the caustic waist region. Owing to diffraction divergence, the length of this beam is proportional to the squared diameter, and increasing the radiation intensity by decreasing the beam diameter results in further shortening of its length.

Focusing the radiation with an axicon (a conical lens) produces a wave beam with a Bessel-type radial field distribution [8–11]. A Bessel beam differs from a Gaussian beam in that the diffraction-induced beam divergence is compensated and its Rayleigh length is theoretically unlimited. As a result, the optical breakdown of substance in the Bessel beam takes the form of an extended filamentary plasma channel [13, 14]. The geometrical beam dimensions and the intensity distribution in the beam are easy to change [12, 15–17]. Owing to these properties of Bessel beams, these channels furnish a unique possibility to change the configuration, parameters, and their distribution, which is important in solving many applied problems.

Every specific task is characterized by its requirements. For instance, short-wavelength plasma lasers [18, 19] necessitate a fast excitation of population inversion. Plasma particle acceleration [14, 20, 21] is possible only for a special optical-discharge propagation mode, for a moving focus. In fast-response laser-triggered switching devices [22–25], the electric conductivity and the shortest channel formation time are primarily important. Energy transfer [12, 26, 27], standard sources, and plasma antennas [28, 29] require a long plasma lifetime.

Recent years have seen the vigorous development of laser-plasma techniques for the generation of radiation in the terahertz range, which is difficult to access (see, e.g., Refs [30–33]), the radiation powered by strong Langmuir oscillations driven by high-intensity laser pulses in the plasma of Bessel beams. One of the prerequisites for the production of strong Langmuir oscillations is the formation of fast ionization fronts. That is why research into the generation of plasma channels was pursued using ultrashort (pico- and femtosecond) laser pulses [34–40].

The properties of plasma channels in gases, liquids, and solids are determined by the heating radiation propagation features of a Bessel beam and its interaction with the propagation medium. In this review, we consider the production of plasma channels in gases.

L N Pyatnitskii Joint Institute for High Temperatures, Russian Academy of Sciences,
ul. Izhorskaya 13, 125412 Moscow, Russian Federation
Tel. (7-495) 485 99 81
Fax (7-495) 485 99 22
E-mail: pyat7@mail.ru

Received 28 February 2009, revised 28 September 2009
Uspekhi Fizicheskikh Nauk **180** (2) 165 – 184 (2010)
DOI: 10.3367/UFNr.0180.201002c.0165
Translated by E N Ragozin; edited by A M Semikhatov

2. Bessel wave beams

The propagation of radiation, specifically electromagnetic radiation, depends on the permittivity ε of the medium. In the general case, the permittivity consists of a linear part, which comprises real ε_0 and imaginary ε'' terms, and the functional ε_{NL}, which takes the special features of the nonlinear matter equations of the propagation medium into account:

$$\varepsilon = \varepsilon_0 + \mathrm{i}\varepsilon'' + \varepsilon_{NL}\left(|\mathbf{E}|^2\right) . \tag{1}$$

Behind an axicon, the axially symmetric field

$$\mathbf{E}(\mathbf{r}, t) = \mathrm{Re}\left\{\mathbf{e}E(r, z)\exp\left[-\mathrm{i}(\omega t - kz)\right]\right\} \tag{2}$$

(where $\mathbf{e}$ is the unit vector of the electric intensity) with an intensity amplitude varying slowly in the propagation direction, z, is defined by the equation [41, 42]

$$2\mathrm{i}k\,\frac{\partial E}{\partial z} + \frac{1}{r}\frac{\partial}{\partial r}\left(r\,\frac{\partial E}{\partial z}\right) + \left(\frac{\omega}{c}\right)^2\left[\mathrm{i}\varepsilon'' + \varepsilon_{\mathrm{NL}}\left(|E|^2\right)\right]E = 0\,, \tag{3}$$

where $k = (\omega/c)\sqrt{\varepsilon_0}$ is the modulus of the wave vector.

The boundary conditions are determined from the geometry of radiation focusing with an axicon with an aperture radius A, which forms a conical wavefront:

$$E(r, z)\Big|_{z=0} = E_{\mathrm{in}}(r)\exp(-\mathrm{i}\mathbf{kr})\,, \tag{4}$$

where $|E_{\mathrm{in}}(r)|_{r>A} = 0$, $|E_{\mathrm{in}}(r)|_{r \leqslant A} = \sqrt{I(r)}$, $I(r)$ is the radial distribution of the initial beam intensity, and $\mathbf{kr} = kr\sin\gamma$. The hyper-Gaussian beam distribution of radius R and order $N \geqslant 1$ has the form

$$E_{\mathrm{in}}(r) = E_{\mathrm{in}}^0\exp\left[-\left(\frac{r}{R}\right)^{2N}\right]. \tag{5}$$

For linear radiation propagation, when $\varepsilon'' = \varepsilon_{\mathrm{NL}} = 0$, the solution $E^{(0)}$ of problem (3) with boundary condition (4) is given by

$$E^{(0)}(r, z) = E_0\exp\left(-\mathrm{i}\,\frac{kz\sin^2\gamma}{2}\right)\left(J_0(x) - \mathrm{i}\,\frac{r}{2z\sin\gamma}\,J_1(x)\right) + E_A\exp\left(\mathrm{i}k\,\frac{A^2 + r^2}{2z}\right)J_0\left(\frac{kAr}{z}\right), \tag{6}$$

where

$$x = kr\sin\gamma\,. \tag{7}$$

Equation (6) holds for the paraxial region $r < z\sin\gamma$, $kr^2 < z$ in the portion $\lambda/\sin^2\gamma \ll z < L_A$ of the axicon focal segment of the length $L_A = A/\tan\gamma$. The first term, correct up to a small quantity of the order of $r/(z\sin\gamma)$, is the field of a nondiverging beam with the wave vector $k_\perp = k\sin\gamma$ normal to the axis [for the variation of its longitudinal part $\delta k_\parallel = (1/2)k\sin^2\gamma$] and with the slowly varying amplitude

$$E_0(z) = 2\pi\sin\gamma\sqrt{\frac{z}{\lambda}}\,E_{\mathrm{in}}(z\sin\gamma)\exp\left(-\mathrm{i}\,\frac{\pi}{4}\right). \tag{8}$$

The second term in the right-hand side of Eqn (6) with the amplitude $E_A = E_{\mathrm{in}}(A)\exp(-\mathrm{i}kA\sin\gamma)/(1 - z/L_A)$ describes the axicon edge diffraction. Its amplitude is lower by the factor $\sqrt{\lambda/z} \ll 1$ than the amplitude of the first term. Because the beam radius normally does not exceed the axicon aperture, $R \leqslant A$, the effect of diffraction on distribution (6) decreases, according to conditions (4) and (5), proportionally to $\exp[-(A/R)^{2N}]$. It follows that axicon focusing for a linear radiation propagation forms a beam wherein the intensity distribution obeys the relation [42]

$$\left|E^{(0)}(r, z)\right|^2 = \left|E_0(z)\right|^2 J_0^2(k_\perp r)\,. \tag{9}$$

In these beams, the radial field distribution is given by the zeroth-order Bessel function J_0 of the first kind. In this case, the axial field distribution $|E_0(z)|$ of the Bessel beam is related to the geometrical-optics factor, which depends mainly on the radial field profile of the initial beam. For the initial radiation profile (5) and an axicon with a rectilinear generatrix, the amplitude of the focused beam field is proportional to $\sqrt{z/\lambda}\,E_{\mathrm{in}}(z\sin\gamma)$.

The specific character of radiation propagation in the case of a nonlinear interaction with a medium is related to the nonlinear part $\varepsilon_{\mathrm{NL}}(|\mathbf{E}|^2)$ of the medium permittivity and its dependence on the intensity of the beam field. In gases, the nonlinearity normally shows up in the breakdown and immediately before it. In this case, a partly ionized plasma emerges, in which the dependence of the permittivity on the field intensity may be local or nonlocal, with and without saturation [42, 43].

In partly ionized plasmas, the resultant electron temperature varies depending on the balance of the energy the electrons acquire due to inverse bremsstrahlung and lose in collisions with neutral particles. When the field nonuniformity scale length l_E is much greater than the electron mean free path $l_{\mathrm{e}} = v_{\mathrm{e}}/v_{\mathrm{en}}$, $l_{\mathrm{e}}/l_E < \sqrt{\delta_{\mathrm{en}}}$, where δ_{en} is the fraction of energy transferred by electrons to neutral particles in the collisions (for elastic collisions, $\delta_{\mathrm{en}} = 2m/M$), the nonlinear part of the permittivity, which is defined by the deviation $\delta n = n - n_0$ of the electron density n from its initial value n_0, is

$$\varepsilon_{\mathrm{NL}} = \frac{-\delta n}{n_{\mathrm{c}}} = \frac{n_0}{n_{\mathrm{c}}}\,\frac{|E|^2/E_T^2}{1 + |E|^2/E_T^2}\,, \tag{10}$$

where $E_T = \sqrt{12\pi\delta_{\mathrm{en}}n_{\mathrm{c}}T_{\mathrm{e}0}}$ is the electric plasma field typical for the thermal nonlinearity, $n_{\mathrm{c}} = m\omega^2/(4\pi e^2)$ is the critical density of electrons, and $T_{\mathrm{e}0}$ is their initial temperature.

In a sufficiently hot plasma, when the electron mean free path exceeds the field gradient scale length, $l_{\mathrm{e}} > l_E$, the electron density varies under the action of the ponderomotive force caused by the striction nonlinearity. In this case, the nonlinearity is also local and the nonlinear part of the permittivity takes the simpler form

$$\varepsilon_{\mathrm{NL}} = \frac{n_0|E|^2}{n_{\mathrm{c}}E_{\mathrm{s}}^2}\,. \tag{11}$$

Expression (11) corresponds to formula (10) under the condition $|E|^2/E_{\mathrm{s}}^2 \ll 1$, but the plasma field $E_{\mathrm{s}} = \sqrt{16\pi n_{\mathrm{c}}T_{\mathrm{e}0}}$ characteristic of the striction nonlinearity is used in (11).

A local power-law nonlinearity is observed not only in plasmas but also in other media in which, in particular, the Kerr effect manifests itself. In gases with excited atoms, the nonlinearity may be due to multiphoton transitions from metastable states. In this case, the nonlinear permittivity may exhibit a higher-power, for instance, quadratic dependence on the field intensity:

$$\varepsilon_{\mathrm{NL}} \sim \frac{|E|^4}{E_{\mathrm{p}}^4}\,. \tag{12}$$

In a partially ionized plasma with a long electron mean free path, when $\sqrt{\delta_{\mathrm{e}}} < l_{\mathrm{e}}/l_E < 1$, the plasma nonlinearity becomes nonlocal. The nonlinear permittivity, as in the case of expression (10), depends on the electron density variation $\delta n = n - n_0$, but the difference δn depends on the electron heat conductivity, which is defined by the equation

$$\frac{2}{3}\,\frac{l_{\mathrm{e}}^2}{\delta_{\mathrm{e}}}\,\Delta\left(\frac{\delta n}{n_{\mathrm{c}}}\right) - \frac{\delta n}{n_{\mathrm{c}}} = \frac{\delta n}{n_{\mathrm{c}}}\,\frac{|E|^2}{E_T^2}\,, \tag{13}$$

where Δ is the Laplace operator. We emphasize that the ionization and recombination frequencies in relations (10) and (13) are assumed to be low in comparison with the inverse electron temperature and the inverse pressure settling time.

In dimensionless variables $\mathscr{E} = E/E^*$ for the field amplitude normalized to the value $E^* = E_{T,p,s}$ characteristic of this type of nonlinearity, we rewrite Eqn (3) as

$$\mathrm{i}\,\frac{\partial \mathscr{E}}{\partial z} + \frac{1}{x}\frac{\partial}{\partial x}\left(x\,\frac{\partial \mathscr{E}}{\partial x}\right) + \left[\mathrm{i}\Gamma + \beta X\right]\mathscr{E} = 0\,, \tag{14}$$

where $\Gamma = \varepsilon''/(\varepsilon_0 \sin^2\gamma)$ is the dimensionless absorption coefficient and $\beta = [n_0/(n_c - n_0)]\sin^{-2}\gamma$. Here, we use notation (7) and the density variation for the local nonlinearity expressed by the ratio

$$X = -\frac{\delta n}{n_0} = \frac{|\mathscr{E}|^2}{1 + |\mathscr{E}|^2}\,, \tag{15}$$

which corresponds to formula (11) when $|\mathscr{E}|^2 \ll 1$:

$$X = |\mathscr{E}|^2\,. \tag{16}$$

In the case of a nonlocal nonlinearity, it follows from Eqn (13) for $\sin^2\gamma \ll 1$ and small spatial derivatives with respect to z that

$$\frac{1}{x}\frac{\partial}{\partial x}\left(x\,\frac{\partial X}{\partial x}\right) + \alpha\left(-|\mathscr{E}|^2 + X\right) = 0\,, \tag{17}$$

where $\alpha = (3/2)\delta_e(kl_e\sin\gamma)^{-2} \ll 1$ and condition (4) becomes $\mathscr{E}(x, z = 0) = \exp(-\mathrm{i}x)$.

Equations (14)–(17) were numerically solved for hyper-Gaussian beam (5) for $N = 8$ and $R < A$. The intensity field at the boundary $x = x_{\max} \approx 10^3 > Ak\sin\gamma = 0.8\,x_{\max}$ of the computation domain and beyond it was taken to be zero, $\mathscr{E}(x,z)_{x \geqslant x_{\max}} = 0$. To match the conditions of these calculations to the experimental ones in [44–47], we used a radial beam distribution $\mathscr{E}_{\mathrm{in}}(x)$ such that the amplitude of linear solution (8) remained constant over the greater part of the focal segment length L_A. The conservation of the energy flux of Eqn (4) served as the solution accuracy criterion.

Numerical investigations under the assumption of linear absorption of the heating radiation, when the optical thickness τ over a distance $s \approx R/\gamma$ is small, $\tau = ks\varepsilon'' < 1$, showed that the structure of the Bessel beam field is hardly different from its structure in the absence of absorption. This condition corresponds to a bound on the radius r of the absorbing domain:

$$\frac{r}{\lambda} < \frac{\gamma}{2\pi}\,\frac{1}{\varepsilon''}\,. \tag{18}$$

For instance, for radiation at the wavelength $\lambda = 1.06$ μm and the angle $\gamma = 0.1$, the effect of dissipation on the beam field in a plasma with the parameters $n_e \sim 10^{19}$ cm^{-2} and $\nu_e \sim 10^{13}$ s^{-1} may be neglected when $r < 100$ μm.

The form of the radial distribution of a Bessel beam may be changed. In essence, the role of an axicon reduces to the transformation $\exp(-\mathrm{i}\mathbf{kr})$, which converts a Gaussian wave beam into a beam with the Bessel radial distribution J_0. An additional azimuthal deflection of the wave vector $\mathbf{k}$, $\exp(-\mathrm{i}s\varphi)$, transforms the distribution J_0 into a Bessel beam with the radial distribution given by a higher-order Bessel function J_n [17, 48]. The vector $\mathbf{k}$ is deflected in the azimuthal direction by adding a phase helix or a kinoform [49], resulting in the formation of a tubular Bessel beam. We now consider the action of the conversion system.

Behind an axicon with a rectilinear generatrix and a relative refractive index N, the angle γ of inclination of the vector $\mathbf{k}$ to the z axis is defined by the refracting angle α, $\gamma = (N-1)\alpha$ (for $\alpha \ll 1$), while the change in the radiation field phase depends on the radius r and the angle α linearly, $\Delta\psi_{\mathrm{A}} = -k(N-1)\alpha r$. The phase helix additionally deflects the wave vector azimuthally by an angle φ. When the phase helix thickness $h(\varphi)$ with a peak h_0 increases linearly as

$$h(\varphi) = \frac{\varphi}{2\pi}\,h_0\,, \tag{19}$$

the variation of the radiation field phase ψ is given by

$$\Delta\psi_{\mathrm{p}} = k(N-1)\,h_0\,\frac{\varphi}{2\pi} = s\varphi\,, \tag{20}$$

where the relative refractive indices of the phase helix and the axicon are assumed to be equal.

On completion of a full turn of the azimuth angle, $\varphi = 2\pi$, converter thickness (19) and phase (20) experience a jump, which produces perturbations due to diffraction and scattering. However, owing to the smallness of these perturbations, the phase variation in (20) can subsequently be treated in the geometrical optics approximation. Under the new conditions, for a wave of type (2), the complex amplitude of the electric field strength of the radiation field is

$$\mathbf{E}(\mathbf{r},t) = \mathrm{Re}\left\{\mathbf{e}E(r,\varphi,z)\exp\left[-\mathrm{i}(\omega t - kz)\right]\right\}, \tag{21}$$

and condition (4) takes the form

$$E(r,\varphi,z)\Big|_{z=0} = E_{\mathrm{in}}(r)\exp\left[-\mathrm{i}(s\varphi - kr\sin\gamma)\right]. \tag{22}$$

We represent the radial field distribution in the incident beam by expression (5), as before.

The field of the focused beam can be described by the wave equation in the parabolic approximation [37]:

$$2\mathrm{i}k\,\frac{\partial E}{\partial z} + \frac{1}{r}\frac{\partial}{\partial r}\left(r\,\frac{\partial E}{\partial r}\right) + \frac{1}{r}\,\frac{\partial^2 E}{\partial\varphi^2} + \left(\frac{\omega}{c}\right)^2\left[\mathrm{i}\varepsilon'' + \varepsilon_{\mathrm{NL}}\left(|E|^2\right)\right]E = 0\,. \tag{23}$$

We represent the radiation field as the sum of azimuthal harmonics:

$$E(r,\varphi,z) = \sum_{m=-\infty}^{\infty} E_m(r,z)\exp(\mathrm{i}m\varphi)\,.$$

With the order-m Fourier–Bessel transform, we obtain the linear ($\varepsilon'' = \varepsilon_{\mathrm{NL}} = 0$) solution of Eqn (23) for the harmonics $E_m(r,z)$:

$$E^{(0)}(r,\varphi,z) = -\mathrm{i}\,\frac{k}{z}\exp\left(\mathrm{i}\,\frac{kr}{2z}\right)\sum_{m=-\infty}^{\infty} B_m(s)\exp\left[\mathrm{i}m\left(\varphi - \frac{\pi}{2}\right)\right] \times \int_0^R E_{\mathrm{in}}(r')\,J_m\left(k\,\frac{r}{z}\,r'\right)\exp\left[\mathrm{i}\psi(r')\right]r'\,\mathrm{d}r'\,. \tag{24}$$

Here,

$$B_m(s) = \frac{\exp\left[2\pi i(s-m)\right] - 1}{2\pi i(s-m)}\,, \qquad \psi(r') = \frac{kr'^2}{2z} - kr'\sin\gamma\,,$$

and $J_m((kr/z)\,r')$ is the mth-order Bessel function.

When the parameter s of phase helix (22) is an integer, $s = n$, solution (24) corresponds to a single azimuthal mode, whose number is defined by the value

$$B_m(s=n) = \delta_{m,m}\,.$$

In the paraxial zone of the Bessel beam $r < z\sin\gamma$, $kr^2 < z$ in the main portion $\lambda/\sin^2\gamma \ll z < L_A$ of the focal segment length $L \approx R/\tan\gamma$, we have the following asymptotic expression for solution (24):

$$E^{(0)}(r,\varphi,z) = \exp\left[in\left(\varphi - \frac{\pi}{2}\right)\right] \times \left[E_0 J_n(kr\sin\gamma)\exp\left(ik\,\frac{r^2 + z^2\sin^2\gamma}{2z}\right) + E_A J_n\left(k\,\frac{rR}{z}\right)\exp\left(-\frac{ik(r^2+R^2)}{2z}\right)\right], \tag{25}$$

where

$$E_0(z) = \sqrt{2\pi kz}\,\sin\gamma\,E_{\text{in}}(z\sin\gamma)\exp\left(-\frac{i\pi}{4}\right),$$

$$E_A = \frac{E_{\text{in}}(A)}{1 - z/L_A}\exp\left(-ikA\sin\gamma\right).$$

The first term in expression (25) is the variation of the complex amplitude of the beam field with the diffraction neglected. The second term describes the axicon edge diffraction. Under the conditions specified in the comment to formula (6), this term is small in comparison with the first term at the ratio $\sqrt{\lambda/z} \ll 1$. Under the approximation adopted here, the radial distribution of the field intensity in the focused beam can be represented as

$$\left|E^{(0)}(r,z)\right|^2 \approx |E_0|^2 J_n^2(kr\sin\gamma)\,. \tag{26}$$

Therefore, for an integer parameter s, a tubular beam forms whose radial field distribution is described by the nth-order Bessel function. Evidently, the order n corresponds to the pitch of the helix that is equal to an integer number of wavelengths,

$$n = \frac{\Delta h}{\lambda}\,(N-1)\sqrt{\varepsilon_0}\,. \tag{27}$$

The nonlinear interaction of the beam field with its propagation medium is defined by the imaginary part ε'' and the nonlinear intensity-dependent term ε_{NL} of permittivity (1). By passing to dimensionless variables, as in Eqn (14), we obtain

$$i\,\frac{\partial\mathscr{E}_n}{\partial z} + \frac{1}{x}\frac{\partial}{\partial x}\left(x\,\frac{\partial\mathscr{E}_n}{\partial x}\right) + \left[i\Gamma + \beta|\mathscr{E}_n|^2 - \frac{n^2}{x^2}\right]\mathscr{E}_n = 0\,. \tag{28}$$

Equation (28) was solved by the procedure of trial and error in radius. Boundary conditions (4) corresponded to the initial Gaussian beam (5) of the order $N = 8$. The field amplitude $E_{\text{in}}(r)$ was profiled in such a way as to make the linear solution amplitude $\mathscr{E}_0(r) = E_0/E^*$ constant throughout the working portion of the focal segment length. The method of calculation, the parameters, and the ranges of their variation were similar to those of problem (14).

Calculations showed that self-modulation in the beams with the J_n initial field distribution occurs, as with J_0, for a power close to the critical power for self-focusing:

$$|\mathscr{E}^{(0)}|^2_{\max} = |\mathscr{E}_c|^2 = \frac{1}{\beta}\,, \tag{29}$$

where β is the dimensionless nonlinearity coefficient from Eqn (28). In this case, the self-modulation for beams with the radial profile J_n differs from the self-modulation for beams with the profile J_0. In the J_n beams, in particular, the instability develops from the beam periphery to its center as the power increases, while in the J_0 beam, perturbations arise on its axis and propagate toward the periphery. In the J_n beams, the modulation is therefore observed not near the first peak, as is the case with the J_0-profile beams, but in the region of higher-order peaks. Furthermore, the structure of the J_n-beam field smears for $r > r_c$ for each mode. This effect becomes stronger with increasing the absorption Γ_0.

3. Optical discharge in the field of a Bessel beam

An axicon transforms a plane wave front of heating radiation to a conical wave front. The vertex of the cone, which is on the symmetry axis at the point $z = 0$, faces the axicon. The wave front propagates along the normal to the cone surface at the speed of light c, and the intersection region of the cone and the z axis travels along this axis with the speed

$$V = \frac{c}{\cos\gamma}\,. \tag{30}$$

Owing to the wave nature of light, a plane front of the Bessel beam forms in the intersection region. This front travels along the z axis with the same speed V, and its motion corresponds to the so-called moving focus regime. The waves of the altered medium state, such as the breakdown, ionization, and population inversion waves, should also propagate in this regime in the Bessel beam. However, the breakdown of the working medium and its attendant processes emerge at the beginning of the focal segment and propagate at constant speed (30) only in the case of a short heating pulse or for a constant intensity along the focal segment of the axicon.

The longitudinal field distribution in the Bessel beam depends on the order N of the initial Gaussian beam and the surface shape of the focusing axicon [12, 50–52]. In the general case, the field increases beginning with the initial part of the focal segment, but it decreases at its end. For example, we consider the propagation of a breakdown wave in this general case. For definiteness, we take an initial hyper-Gaussian beam of the order $N = 5$ and an axicon with a rectilinear generatrix. The intensity distribution $I(z)$ along the focal segment in these conditions is shown in Fig. 1a. The dashed line I_{th} corresponds to the level of the breakdown threshold for the propagation medium.

A discharge originates at the point z_1 and terminates at the point z_2. Behind the z_2 point, the intensity is insufficiently high for breakdown and the discharge propagation terminates. When the energy of the heating pulse is high enough, an

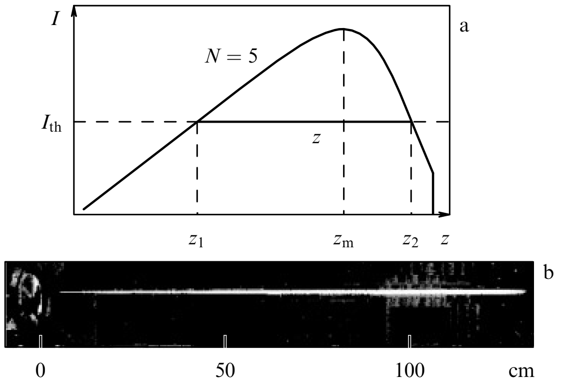

Figure 1. Optical discharge limits (a) and plasma channel in a Bessel beam (b): $\lambda = 1.06$ μm, $D = 4.5$ cm, $d = 50$ μm, $\tau = 50$ ns, $E = 200$ J, $\gamma = 1°$, the air at 1 atm.

extended plasma channel forms in the segment $Z = z_2 - z_1 < L$. Its photograph is shown in Fig. 1b. The Bessel beam with the diameter $d = 50$ μm and length $Z = 1.3$ m was produced by a laser pulse with the duration $\tau = 50$ ns and the energy $E = 200$ J, which had the form of a Gaussian beam ($\lambda = 1.06$ μm, $N = 5$, and $D = 4.5$ cm) and was transformed by an axicon with a rectilinear generatrix and the angle $\gamma = 1°$.

In a Bessel beam, the translational motion of the discharge boundary from z_1 to z_2 with the speed V defined by relation (30) is not always possible. This is true only when the rise time τ of the heating pulse [i.e., the time of the intensity increase to the level $(1 - 1/\mathrm{e}^2)$ of its peak value] is shorter than the time of its propagation through the focal segment L:

$$\tau \ll \frac{L}{c}\cos\gamma\,. \tag{31}$$

The focal segment length L itself depends on the angle γ, $L = R\tan\gamma$, and hence

$$\tau \ll \frac{R}{c}\,\frac{\cos^2\gamma}{\sin\gamma}\,. \tag{32}$$

Inequality (32), which limits the rise time, is highly sensitive to the angle γ, and the leading edge of the heating pulse should become steeper as this angle decreases. In view of these features of propagation of the pulse front, this regime of optical discharge formation is termed dynamic. The opposite, quasistatic, regime is characterized by a slow increase in the radiation intensity, with

$$\tau \gg \frac{L}{c}\cos\gamma\,. \tag{33}$$

Under condition (33), the length of the heating radiation wave train turns out to be longer than the focal segment. That is why the instantaneous longitudinal field distribution over the focal segment is virtually coincident with the dependence depicted in Fig. 1a. Accordingly, only the scale of the distribution amplitude varies with time. In this quasistatic regime, as is clear from Fig. 1a, the beam field reaches the breakdown threshold at the point of the distribution peak z_{m} first. As the field amplitude increases, the discharge length Z is bounded, as before, by coordinates z_1 and z_2, which depend on the power of the heating pulse. However, unlike the discharge in the previous regime, the discharge that originates at the point z_{m} where the field reaches its peak value propagates in both directions.

In this regime, the discharge propagation speed is defined not by relation (30) but by the slope of the $I(z)$ curve, which is different on opposite sides of the z_{m} point. In the region $z > z_{\mathrm{m}}$, the speed is below the speed of discharge propagation in opposition to the radiation, $z < z_{\mathrm{m}}$; in both directions, the speed increases with increasing the heating pulse energy. The position of the peak z_{m} depends on N. Under the conditions involved, z_{m} is rather accurately described by the expression

$$\frac{z_{\mathrm{m}}}{L} \approx 0.5\,N^{0.24}\,. \tag{34}$$

The relative discharge length Z/L also depends on N. In this case, as the refracting axicon angle α decreases, reaching the breakdown threshold requires higher-energy heating pulses owing to an increase in the axicon caustic length L. But for every refracting angle, strengthening the heating pulse leads to an increase in the optical discharge length Z within the bounds of the focal segment L, $(Z/L) \to 1$.

Once the intensity $I(z,t)$ at the peak of the beam field reaches the breakdown magnitude $I(z_{\mathrm{m}}, t_{\mathrm{m}}) = I_{\mathrm{th}}$, a discharge in the neighborhood of the z_{m} point emerges, $Z = z_2 - z_1 \approx 0$. Increasing the pulse energy and intensity has the effect that the points z_1 and z_2 shift apart and the discharge length increases. When the intensity level I_{th} is known, determining the velocity of travel of these points requires specifying the function $I(z,t)$. Under condition (33), the arguments of this function separate and it may be represented in a factored form:

$$I(z,t) = I(z)\,f(t)\,. \tag{35}$$

A breakdown normally originates at the leading edge of the function $f(t)$, whose temporal run may be represented by the expression $f(t) = I_0\left(1 - \exp\left[-(t/\tau)^2\right]\right)$, where I_0 is its peak value. Because of the form of the $I(z,t)$ function, the solution of this basically simple problem entails cumbersome calculations, which involve solving an equation of the type $y = x\exp x$. Another complication is related to properties of the Gaussian function and the uncertainty in selecting the zero time. We somewhat simplify this function to avoid cumbersome calculations.

The dependence $I(z)$ is approximated by a triangle with the vertex at the point $z_{\mathrm{m}} = 0.5\,N^{0.24}$ and of the height that varies in time as $I_{\mathrm{m}} = I_0 f(t)$. It suffices to transform the function $f(t)$ in the initial region, where $f(t) \ll 1$ and $I \ll I_{\mathrm{m}}$ does not exert an effect on the interaction of radiation with the propagation medium. For this, in the range from $t/\tau = -\infty$ to the inflection point $t/\tau = -\sqrt{2}/2$, we replace the Gaussian function by a straight line passing through this point with the slope $\tan\varphi = \sqrt{2/\mathrm{e}}$ and place the origin at the point $t/\tau = -1.4$. The function $f(t)$ may now be represented by two expressions relating to the two time intervals:

$$f(t) = \begin{cases} \sqrt{\dfrac{2}{\mathrm{e}}}\left(\dfrac{t}{\tau} - 1.4\right) - \dfrac{2}{\sqrt{\mathrm{e}}}\,, & \dfrac{t}{\tau} \in \left[0,\ 1.4 - \dfrac{\sqrt{2}}{2}\right], \\ \exp\left[-\left(\dfrac{t}{\tau} - 1.4\right)^2\right], & \dfrac{t}{\tau} \in \left[1.4 - \dfrac{\sqrt{2}}{2}\,,\ 1.4\right]. \end{cases} \tag{36}$$

The derivatives of expressions (36) define the rate of intensity build-up at an arbitrary point of the focal segment. From the condition $I(z,t) = I_{\mathrm{th}}$ with the known $I(z)$ and I_{th}, we then obtain the dependence of the velocities of breakdown

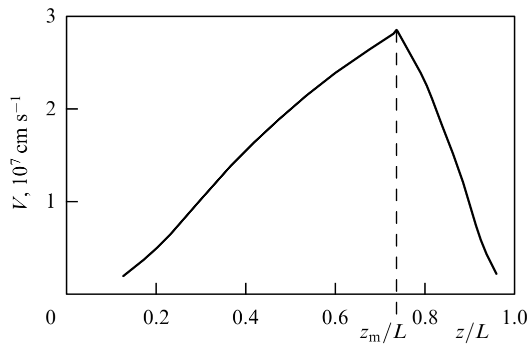

Figure 2. Discharge propagation velocities in quasistatic regime (32), with $N = 5$ and $I_m/I_{th} = 5$.

boundary propagation from the z_m point in two directions along the focal segment. This dependence is exemplified for $N = 5$ and $I_m/I_{th} = 5$ in Fig. 2. We note that the discharge plasma of the Bessel beam absorbs only a small fraction of the energy of the heating laser pulse when its energy is not high and $Z/L < 1$. As $Z/L \to 1$, the radiation-use efficiency increases and may exceed 90%.

Because a long Rayleigh length is inherent in a Bessel beam, the resultant optical-discharge plasma has the shape of an extended plasma channel. The emergence of the channel and the plasma-induced absorption of the heating radiation entail an increase in temperature and pressure in the volume of the Bessel beam. In accordance with the beam shape, this volume begins to play the role of a cylindrically shaped piston whose motion generates a cylindrical shock wave [53, 54].

4. The plasma channel and its development

At the instant of plasma channel inception, the positions of the shock wave and the plasma piston surface coincide. Subsequently, the shock wave leaves the piston behind. Behind the shock, a domain of perturbed gas flow forms (the channel shell according to Ref. [55]). The channel broadening from the instant of its inception to the instant of shock separation may be estimated using the self-similar solution for an instantaneous strong explosion of a cylindrical configuration [56].

The velocity u, density ρ, pressure p, and temperature T of the gas behind the shock propagating through an immobile gas are described by the formulas

$$
\begin{aligned}
u &= \frac{2}{\gamma+1}\, D\left(1 - \frac{c^2}{D^2}\right) = \frac{2}{\gamma+1}\, D f_1 \,, \\
\rho &= \frac{\gamma-1}{\gamma+1}\, \rho_0 \left(1 + \frac{2}{\gamma-1}\frac{c^2}{D^2}\right) = \frac{\gamma+1}{\gamma-1}\, \rho_0 f_2 \,, \\
p &= \frac{2}{\gamma+1}\, \rho_0 D^2 \left(1 - \frac{\gamma-1}{2\gamma}\frac{c^2}{D^2}\right) = \frac{2}{\gamma+1}\, \rho_0 D^2 f_3 \,, \\
T &= \frac{p}{R\rho} \,,
\end{aligned}
\tag{37}
$$

where ρ_0 and c are the gas density and the speed of sound in front of the shock, D is the shock speed, γ is the effective adiabatic exponent, and R is the gas constant. The correction functions f_1, f_2, and f_3, which take the counterpressure into account, depend on the ratio c/D and are equal to unity for $c/D = 0$: $f_1 = f_2 = f_3 = 1$. When the channel expansion speed is known, the temperature step behind the shock front is given by

$$
T = \frac{2(\gamma-1)}{R(\gamma+1)^2}\, D^2 \,. \tag{38}
$$

On the other hand, the radius r of a cylindrical shock and its speed D are expressed in terms of the explosion energy E per unit channel length:

$$
\begin{aligned}
r &= \left(\frac{Et^2}{\rho_0}\right)^{1/4} , \\
D &= \frac{1}{2r}\sqrt{\frac{E}{\rho_0}} \,,
\end{aligned}
\tag{39}
$$

or

$$
D = \frac{r}{2t} \,. \tag{40}
$$

When an energy E_0 falls on a unit length of a Bessel beam, the effective linear energy deposition is $E = \alpha E_0$. The value of E required for the calculation can be estimated using the experimentally known ratio between the plasma channel length Z and the focal segment L. But a comparison of theoretical curves and experimental data suggests that the self-similar solution provides an insufficiently accurate description of the experimentally observed motion of a cylindrical shock wave.

This may be attributed to the following circumstances. First, for a small diameter of the channel, a heating pulse of nanosecond duration cannot be considered instantaneous, which is the premise for applying the theory of a strong point-like explosion. Second, the high temperature of the plasma leads to substantial losses of specific energy for radiation and ionization. Furthermore, the explosion propagation depends on the counterpressure, and the channel expansion velocity during the action of the heating pulse may be affected by laser-supported detonation.

The temperature of the plasma channel can also be estimated by setting the radial channel expansion speed equal to the ion sound speed c in the plasma (this method was applied to investigations of the properties of an optical discharge at the focus of a spherical lens [57]):

$$
D \approx c = \sqrt{\gamma(\gamma-1)\mathcal{E}} \sim \sqrt{\frac{T}{m_i}} \,, \tag{41}
$$

where $\mathcal{E}$ is the specific energy, γ is the effective adiabatic exponent, and m_i is the ion mass. In the calculation of the sound speed in Ref. [57], the values of the adiabatic exponent were borrowed from the tables in Ref. [58].

In reality, the state of equilibrium in a laser-produced plasma is unknown. If the plasma is assumed to be in equilibrium, calculations yield somewhat overestimated density and pressure values and an underestimated temperature value. That is why in many papers concerned with the theoretical investigation of explosion processes in gases with axially symmetric energy sources (see, e.g., Refs [59–66]), deviations from equilibrium are taken into account along with other real processes.

The development of a plasma channel in the field of a Bessel beam was numerically investigated in Ref. [66]. The zeroth-order Bessel beam was formed by a profiled axicon, which produced a constant intensity on the axis along the focal segment. The central axial beam caustic was considered, in which the intensity is highest. A strong thermal explosion was produced in the air by a laser pulse of nanosecond duration. For definiteness, the initial radius of the interaction domain was limited to the interval 0.002–0.1 cm. During the course of the heating radiation, the gas in the volume of the Bessel beam was heated to a temperature exceeding its initial value by a factor of several hundred.

Because the durations of the heating pulse and the main elementary processes in the optical discharge are much shorter than the characteristic gasdynamic times, the solution of this problem splits into two stages, kinetic and gasdynamic. The composition, temperature, component densities and other local plasma parameters are determined by the end of the pulse action. To calculate them, the mathematical IKAR model was used [67]. At the second stage, the HERA-θ code package [68] was used to investigate the dynamics of the initial development stage of the channel, which was treated as an axially symmetric thermal explosion. Several modifications introduced into this model are described in Ref. [67].

The gasdynamics of the cylindrical plasma channel were numerically investigated for nitrogen. The results of these calculations may also be carried over to the air, because optical discharges in nitrogen and dry air, according to the measurements in Refs [69, 70], induced by laser radiation ($\lambda = 1.06$ μm) for the intensity $\sim 10^{11}$ W cm^{-2} and pulse duration $\tau = 1-10$ ns develop in about the same manner in a wide pressure range.

In addition to the model in Ref. [67], the following factors were taken into account in kinetic calculations: plasma heating due to the energy transfer of the internal degrees of freedom of excited molecules, atoms, and ions to translational and rotational degrees of freedom; the nonequilibrium character of the electron energy distribution function; the excitation of the metastable atoms $N(^2D^0)$ and $N(^2P^0)$ and the ions $N^+(^1D)$; the quenching of excited particles in collisions with electrons; the V−T relaxation and thermal dissociation of molecules and the complex ions N_3^+ and N_4^+; and multiphoton processes [71, 72].

The temperatures T_a of heavy particles were assumed to be equal; this temperature was found from the energy balance equation that included the energy transfer from electrons to heavy particles. Because the photon energy $\hbar\omega = 1.17$ eV is small in comparison with the electron energy, the electron distribution was found from the classical kinetic equation [73–77]:

$$\alpha f(\epsilon) = \frac{1}{\sqrt{\epsilon}} \frac{d}{d\epsilon} \left\{ \epsilon^{3/2} \left[\frac{2}{3}\, \epsilon_0 \nu_{\rm eff} \frac{\partial(P/\rho)}{\partial\epsilon} + \delta f(\epsilon) + T_a \frac{\partial(P/\rho)}{\partial\epsilon} \right] \right\} + S_{\rm in} + S_{\rm ee}\,, \tag{42}$$

where

$$\alpha = \frac{1}{n_e}\frac{dn_e}{dt}\,, \qquad \epsilon = \frac{4\pi e^2 G}{mc(\omega^2 + \nu_{\rm eff}^2)}\,,$$

G is a coefficient that takes the radiation loss into account,

$$\nu_{\rm eff} = \nu_{\rm tr} + \nu_{\rm ei}\,, \qquad \delta = \sum_k \frac{2m}{m_k}\, \nu_{ek}\,,$$

ν_{ek} is the elastic collision frequency, and $\nu_{\rm ei}$ is the electron–ion collision frequency.

The collisional term $S_{\rm in}$ in Eqn (42) accounts for the inelastic energy loss due to excitation $S_{\rm ex}$, ionization $S_{\rm ion}$, and dissociation $S_{\rm dis}$:

$$S_{\rm in} = S_{\rm ex} + S_{\rm ion} + S_{\rm dis}\,, \tag{43}$$

$$S_{\rm ex} = \sum_{k,\, i>j} n_j^k \sigma_{ji}^k(\epsilon + I_{ij}^k)\, v(\epsilon + I_{ji}^k) \sqrt{1 + \frac{I_{ji}^k}{\epsilon}} - f(\epsilon)\, v(\epsilon) \sum_{k,\, i>j} n_j^k \sigma_{ji}^k(\epsilon)\,, \tag{44}$$

$$S_{\rm ion} = \sum_{k,j} n_j^k \sigma_{jk}^{\rm ion}(\epsilon + I_{jk}^{\rm ion})\, f(\epsilon + I_{jk}^{\rm ion})\, v(\epsilon + I_{jk}^{\rm ion}) \sqrt{1 + \frac{I_{jk}^{\rm ion}}{\epsilon}} - f(\epsilon)\, v(\epsilon) \sum_{k,j} n_j^k \sigma_{jk}^{\rm ion}(\epsilon) + \alpha\delta(\epsilon) \int_0^\infty f(\epsilon') \sqrt{\frac{\epsilon'}{\epsilon}}\, d\epsilon'\,, \tag{45}$$

$$S_{\rm dis} = \sum_{k,j} n_j^k \sigma_{jk}^{\rm dis}(\epsilon + I_{jk}^{\rm dis})\, f(\epsilon + I_{jk}^{\rm dis})\, v(\epsilon + I_{jk}^{\rm dis}) \sqrt{1 + \frac{I_{jk}^{\rm dis}}{\epsilon}} - f(\epsilon)\, v(\epsilon) \sum_{k,j} n_j^k \sigma_{jk}^{\rm dis}(\epsilon)\,. \tag{46}$$

Here, m and m_k are the electron and k-type particle masses; n_j^k is the density of the k-type particles in the jth energy state; $v(\epsilon)$ is the speed of electrons with an energy ϵ; ϵ_0 is the electron oscillation energy; $\nu_{\rm tr}$ is the frequency of electron collisions with heavy particles; σ_{ji}^k, $\sigma_{jk}^{\rm ion}$, and $\sigma_{jk}^{\rm dis}$ are the excitation, ionization, and dissociation cross sections for k-type particles; and I_{ji}^k, $I_{jk}^{\rm ion}$, and $I_{jk}^{\rm dis}$ are the thresholds for the inelastic processes. The term $S_{\rm ee}$, which accounts for electron–electron collisions, has the form [76]

$$S_{\rm ee} = \frac{1}{\sqrt{\epsilon}} \frac{d}{d\epsilon} \left\{ 2\epsilon^{3/2} \nu_e(\epsilon) \left[\left(f(\epsilon) \int_0^\epsilon f(\epsilon')\sqrt{\epsilon'}\, d\epsilon' \right) + \frac{2}{3} \frac{df}{d\epsilon} \left(\int_0^\epsilon (\epsilon')^{3/2} f(\epsilon')\, d\epsilon' + \epsilon^{3/2} \int_\epsilon^\infty f(\epsilon')\, d\epsilon' \right) \right] \right\},$$

where $\nu_e(\epsilon) = \pi e^4 \Lambda n_e / (\sqrt{2m}\, \epsilon^{3/2})$ is the electron–electron collision frequency and Λ is the Coulomb logarithm. For the Maxwell electron distribution, the expression for $S_{\rm ee}$ simplifies to

$$S_{\rm ee} = \frac{1}{\sqrt{\epsilon}} \frac{d}{d\epsilon} \left\{ 2\epsilon^{3/2} \nu_e(\epsilon) \left[f(\epsilon) + T_{\rm eff} \frac{df}{d\epsilon} \right] \right\},$$

where $T_{\rm eff} = (2/3)\langle\epsilon\rangle \equiv (2/3)\int_0^\infty f(\epsilon)\epsilon^{3/2}\, d\epsilon$ is the effective electron temperature and $\langle\epsilon\rangle$ is the average energy of electrons.

It is assumed that electron escape from the discharge volume may be neglected [73, 74] and the distribution function in Eqn (42) is independent of spatial coordinates, i.e.,

$$\alpha\tau_\alpha \gg 1\,, \tag{47}$$

where $\tau_\alpha \approx 3r_a^2 \nu_{\rm eff} / (2v^2(\epsilon))$ is the mean electron residence time in the Bessel beam volume. According to estimates, for the density of nitrogen molecules 10^{19} cm^{-3}, $r_a \geqslant 0.01$ cm, and $\epsilon_0 \geqslant 10^{-4}$ eV, inequality (47) holds for the most important part of the electron energy spectrum $0 < \epsilon \leqslant 1$ keV.

In Eqn (42), which is a quasistationary approximation, the function responsible for the electron distribution is given by the product

$$F(\epsilon, G, t) = n_{\rm e}(t) f(\epsilon, G) \,. \tag{48}$$

This representation is admissible if the electron distribution relaxation time is much shorter than the time of significant variation of the heating radiation intensity. Representation (48) can be used because the rate coefficients for elementary processes depend only slightly on the corrections to the distribution $f(\epsilon)$ that arise from the variations of the function $G(t)$ during the period when these variations are most significant. This condition is satisfied in the experiments under consideration. In this case, however, the distribution $f(\epsilon)$ is to be calculated anew for different time instants.

The data of calculations of the heating radiation–plasma interaction suggest that the electron energy distribution function is substantially nonequilibrium and is considerably different from the Maxwellian one above some energy $\epsilon(t_1) \sim 20$ eV. This has the effect that an ionization overheating instability develops in the resultant plasma and the plasma temperature increases significantly. This increase depends on the energy input, the pulse shape and duration, and the radius and profile of the field in the energy deposition domain. Upon completion of the pulse, the electrons rapidly become Maxwellian and acquire the temperature of heavy particles.

The energy deposition in the beam generates a radial flow. In Lagrangian coordinates m and t, where m is the mass of the gas column confined to the azimuthal angle equal to one radian at a unit distance from the symmetry axis, this flow is described by the system of equations

$$\begin{aligned} &\frac{\partial u}{\partial t} = -r\,\frac{\partial P}{\partial m}\,, \\ &\frac{\partial r}{\partial t} = u(m,t)\,, \\ &\frac{\partial \mathcal{E}}{\partial t} = -P\,\frac{\partial}{\partial t}\left(\frac{1}{\rho}\right) - \frac{\partial q}{\partial m} + Q\,, \\ &q = -\kappa c r\,\frac{\partial T}{\partial m}\,, \end{aligned} \tag{49}$$

where u is the speed, P is the gasdynamic pressure, $\mathcal{E}$ is the internal energy of a unit gas mass without vibrational energy, q is the heat flux across the transverse section, Q is the mass density of the absorbed heating-radiation density, T is the translational gas temperature, and $\kappa(\rho, T)$ is the thermal conductivity coefficient. The mass coordinate m is related to the Eulerian spatial coordinate r as $\mathrm{d}m = r\rho\,\mathrm{d}r$, where ρ is the gas density, $0 \leqslant m \leqslant M$. The quantity M remains invariable in time. The gas column is assumed to be sufficiently long, i.e., the spatial coordinate r does not exceed the value $r^*(t) \equiv r(M,t)$, $0 \leqslant r \leqslant r(M,t)$, during the selected time interval.

The boundary conditions of the system of equations (49) are defined by the cylindrical symmetry of the problem, $r = 0$, $u(0,t) = 0$, $q(0,t) = 0$, and by the values of unperturbed gas parameters at the outer channel boundary. The local thermodynamic equilibrium in the plasma establishes in several nanoseconds owing to a high electron density, of the order of 10^{19} cm^{-3}. Gasdynamic processes start at the instant t_0 the energy release terminates, when the plasma temperature $T(r, t_0)$ and density $\rho(r, t_0)$ are determined by the calculations of its local characteristics.

The system of equations (49) is not closed and should be supplemented with the equation of state and the expressions for the thermal conductivity coefficient and the energy source. The equation of state for the plasma of dry air is used in the form [63, 64]

$$P = \rho R T\left[1 + A_0 + 2(A_1 + A_2)\right], \qquad 0 \leqslant A_i \leqslant 1\,, \tag{50}$$

$$\mathcal{E} = RT\left[0.5(5 + A_0) + 3(A_1 + A_2)\right] + A_0 I_0 + A_1 I_1 + A_2 I_2\,, \tag{51}$$

$$\begin{aligned} &A_0 = 2\left[1 + (1 + 2B_0)^{1/2}\right]^{-1}, \\ &B_0 = C_0 \rho T^{-1/2} \exp\frac{I_0}{RT}\,, \\ &A_1 = 2\left[1 + (1 + 2B_1)^{1/2}\right]^{-1}, \\ &B_1 = C_1 \rho T^{-3/2} \exp\frac{I_1}{2RT}\,, \\ &A_2 = 2\left[1 + B_2 + (1 + 6B_2 + B_2^2)^{1/2}\right]^{-1}, \\ &B_2 = C_2 \rho T^{-3/2} \exp\frac{I_2}{2RT}\,. \end{aligned} \tag{52}$$

The I_i are the effective specific energies of dissociation $(i = 0)$, and the first $(i = 1)$ and second $(i = 2)$ ionization, the C_i are the corresponding constants in the Saha equation, and $R = 2.871 \times 10^6$ erg (g K)$^{-1}$ is the specific gas constant. The following values are taken for unperturbed gas parameters: $\mu = 28.96$ (molecular weight), $T_0 = 300$ K, $P_0 = 1.01325 \times 10^6$ dyn cm^{-2}, and $\rho_0 = 1.17681 \times 10^{-3}$ g cm^{-3}.

The thermal conductivity coefficient is given by the sum [76]

$$\kappa = \kappa_0 + \kappa_{\rm r} + \kappa_{\rm e}\ [\text{erg cm}^{-1}\ \text{s}^{-1}\ \text{K}^{-1}]\,,$$

where $\kappa_0 = 1000(1 - A_1)\sqrt{T}$ accounts for the thermal conductivity of neutral particles, $\kappa_{\rm r} = 2.2 \times 10^{13} \rho (\mathrm{d}A_0/\mathrm{d}T)$ for the thermal conductivity due to the diffusion of atomic recombination energy, and $\kappa_{\rm e} = 0.1488\sigma T$ for the electron thermal conductivity, where

$$\sigma = \frac{4.173 \times 10^{-10}(A_1 + A_2) T^{1/2}}{2 \times 10^{-15}(1 - A_1) + A_1 b_{\rm ei}}\,,$$

is the electric conductivity [Ω^{-1} cm^{-1}] and

$$b_{\rm ei} = 2.8 \times 10^{-6}\, T^{-2} \left(\frac{A_1 + 3A_2}{A_1 + A_2}\right)^2 \times \ln\left[1.727 \times 10^{-5}\,\frac{A_1 + A_2}{A_1 + 3A_2}\,T\,(A_1\rho)^{-1/3}\right]$$

is the mean cross section of electron–ion collisions [cm^2].

The system of equations (49) supplemented with expressions (50)–(52) is solved under the conditions that the gas temperature, which is equal to T_0 at t_0, increases to $T_{\rm a}$ within the volume of the Bessel beam (a cylinder with a radius r_0). The medium remains unperturbed outside the cylinder:

$$T(r, t_0) = \begin{cases} T_{\rm a}\,, & r \leqslant r_0\,, \\ T_0\,, & r > r_0\,. \end{cases} \tag{53}$$

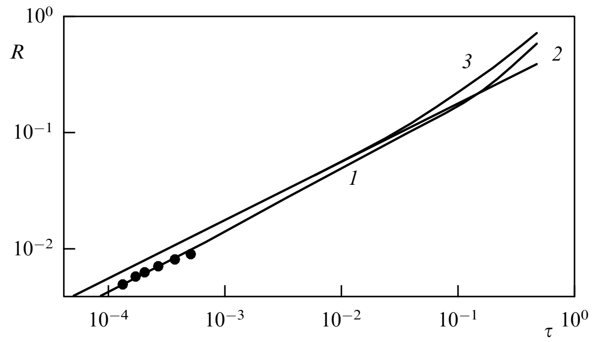

Figure 3. Channel radius vs time in dimensionless coordinates $R = r/r_{\rm m}$ and $\tau = t/\tau_{\rm m}$: kinetic gasdynamic model (curve *1*), cylindrical explosion without counterpressure (curve *2*) and with counterpressure (curve *3*); the dots show experimental data.

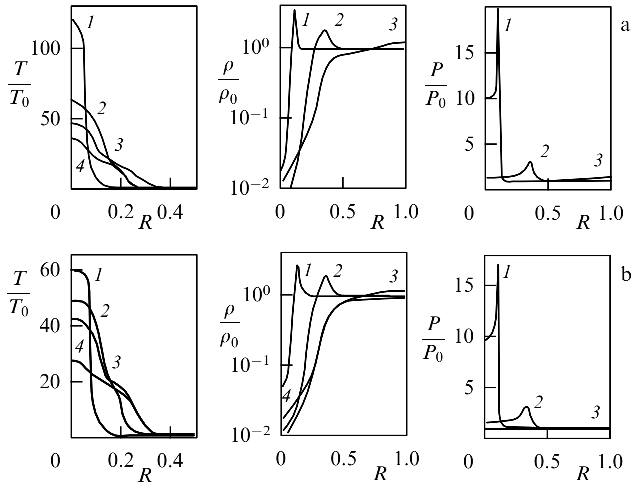

Figure 4. Radial parameter profiles: (a) $r_{\rm m} = 0.01$ cm, $T_{\rm a} = 10$ eV, $E = 0.23$ J cm^{-1}: *1* — $\tau = 0.0109$, *2* — $\tau = 0.1043$, *3* — $\tau = 0.5701$, *4* — $\tau = 1.001$; (b) $r_{\rm m} = 0.0189$ cm, $T_{\rm a} = 3$ eV, $E = 0.23$ J cm^{-1}: *1* — $\tau = 0.0114$, *2* — $\tau = 0.022$, *3* — $\tau = 0.5201$, *4* — $\tau = 1.190$.

Owing to strong temperature gradients, the electron thermal conduction plays a significant role and is included in the calculations. Under the condition $\operatorname{div}(\kappa\nabla T) > \operatorname{div}\mathbf{S}$ (where $\mathbf{S}$ is the radiant energy flux), which is true for high-density plasma at the initial stage of its cooling (up to 100 μs), the radiative heat conductivity may be neglected, as is done, for instance, in the investigation of an electric spark discharge [77, 78].

Figure 3 shows the temporal dependences of the shock wave radius R determined in the framework of the model described above (curve *1*) for a cylindrical point-like explosion without the inclusion (curve *2*) and with the inclusion (curve *3*) of counterpressure for the adiabatic exponent $\gamma = 1.4$. The points reproduce the measured values of the radius of the plasma channel glow domain [79].The curves were plotted for a specific energy input $E = 4$ J cm^{-1} in the dimensionless variables $R = r/r_{\rm m}$ and $\tau = t/\tau_{\rm m}$ [56]:

$$r_{\rm m} = \sqrt{\frac{E}{P_0}}\,, \qquad \tau_{\rm m} = r_{\rm m}\sqrt{\frac{\rho_0}{P_0}}\,. \tag{54}$$

It is evident from Fig. 3 that in a wide range of channel radii and temperatures, the calculated data are rather close to the results of the theory of a point-like explosion with counterpressure but do not exactly coincide with them. At the same time, the experimental points indicating the dimensions of the expanding plasma glow domain coincide with the calculated values of the radius of the shock wave up to the instant of its separation, $\tau \sim 9 \times 10^{-4}$, when the shock wave begins to travel faster than the glow boundary. As regards the plasma parameters, the plasma temperature in particular, their radial distribution is appreciably different from the predictions of the point-like explosion theory.

In this case, the distribution depends not only on the specific energy input but also on the radius r_0 and the temperature $T_{\rm a}$. The radial temperature, density, and pressure profiles at $E = 0.23$ J cm^{-1} are shown for $r_{\rm m} = 0.01$ cm, $T_{\rm a} = 10$ eV (Fig. 4a) and for $r_{\rm m} = 1.89 \times 10^{-2}$ cm, $T_{\rm a} = 3$ eV (Fig. 4b). The relative parameter values are plotted as functions of the dimensionless radius R for several time instants t.

We see from the above examples that the substantial difference in $r_{\rm m}$ and $T_{\rm a}$ has almost no effect on the position of the shock front, but it affects the dynamics and the character of parameter distributions. In particular, in the version depicted in Fig. 4a, the temperature and density on the channel axis, which are significant in practice, change several times faster than the parameters plotted in Fig. 4b. Furthermore, in the former version, the temperature decreases by the factor $(T/T_0)_1/(T/T_0)_4 = 3.4$ and the density to the level $(\rho/\rho_0)_1/(\rho/\rho_0)_4 = 5 \times 10^{-3}$ during the time interval under investigation. In the latter version, these ratios are $(T/T_0)_1/(T/T_0)_4 = 2.14$ and $(\rho/\rho_0)_1/(\rho/\rho_0)_4 = 7.5 \times 10^{-3}$.

From a comparison of the data given above it can be inferred that for the shorter radius $r_{\rm m}$ and the higher temperature $T_{\rm a}$, the parameters exhibit a one-and-a-half times greater variation, while the respective lifetimes of the reduced-density channel in these two cases are $0.023 \leqslant \tau \leqslant 0.82$ and $0.12 \leqslant \tau \leqslant 0.78$. Therefore, by selecting the values of r_0, $T_{\rm a}$, and E, it is possible to control the rarefaction in the channel and its lifetime.

In wave beams with the radial field distribution given by the Bessel function J_n $(n > 0)$, the plasma channel immediately assumes a tubular shape [17, 48, 80–86]. Initially, there is no plasma on the channel axis; the plasma emerges there only after the arrival of an axially converging cylindrical shock wave. The plasma is then strongly compressed. The compression ratio is determined by the order n of the Bessel function and the symmetry of the cylindrical shock wave, which depends on the quality of alignment of the axicon and the phase helix. Subsequently, the strong compression of the paraxial plasma is succeeded by its substantial rarefaction and recompression. On a longer time scale, the alternation of regimes dies down.

5. Optical discharge structures in a Bessel beam

As noted above, the basically unavoidable diffraction divergence of a wave beam, with the angle $\gamma \sim \lambda/d$, where d is the diameter and λ is the wavelength, is compensated when the radiation is focused by forming a conical wave front that converges to the symmetry axis with the angle γ equal to the divergence angle.

Figure 1b shows a photograph of a channel produced under these conditions, which was recorded in the light of plasma emission [87, 88]. The plasma channel of the wave beam rapidly becomes uniform, but at the instant of its inception, the channel structure depends to a large extent on the optical discharge structure, which is defined by the features of the Bessel beam. We therefore consider the structure of discharges that were observed under different conditions in experiments with Bessel beams.

In these experiments, the angle γ was varied from 1° to 18°, which defined the Bessel beam diameter $d \in [3, 50]$ μm and length $L \in [1.5, 130]$ cm. These investigations were carried out in ten different gases at pressures 0.05–10 atm. The heating pulse duration was consecutively shortened from 50 ns to 0.1 ns. The energy of the heating pulse was decreased from 200 J to 0.6 J and the power accordingly increased. The discharge structure was visualized in the light of plasma emission and scattered heating radiation, as well as with the use of shadow and schlieren methods. In experiments involving 0.1 ns long heating pulses, the channel state was investigated by interferometric techniques with laser illumination at a wavelength shorter than that of the heating radiation. The images of transitory structures were recorded using streak and CCD cameras.

It was anticipated that a uniform filamentary plasma channel would emerge owing to the axially symmetric power supply to the focal region in the high-intensity beam with the Bessel field distribution. Even in the first experiments with a laser energy source, however, the resultant plasma exhibited a sequence of axially located perturbations resembling beads [11–14, 89–91]. Initially, the 'beads' were assumed to arise from the complex mode composition of the laser radiation. But investigations involving a single-frequency laser [46] yielded precisely the same result. Therefore, the bead structure of the plasma channel in the beam with divergence compensation was ascribed to the specific features of the optical discharge and the nonlinear propagation of the wave beam itself [41].

The observed structures were classified and the prerequisites to their emergence were analyzed [87, 92]. Five typical structures were singled out; these are depicted in Fig. 5 in the order of their production. In the photographs in Fig. 5, the wave front propagates from left to right.

Figure 5a shows an optical discharge formed in air at the atmospheric pressure by an axicon with $\gamma = 7.5°$ ($L = 17$ cm) for the pulse duration $\tau = 40$ ns and the energy $E = 70$ J. To the special features of the structure must be added the occurrence of lobes that deviate from the symmetry axis, reminiscent of a herring-bone pattern. The lobe bases make up breakdown nuclei (beads) periodically located on the axis and spaced at intervals $l = 0.12$ mm. The inclination β of these lobes to the beam axis is much greater than the γ angle, $\beta \gg \gamma$. Therefore, their occurrence cannot be attributed to the motion of discharge in opposition to the heating radiation, as in optical discharges in the focus of a spherical lens. The lobes are axially located and spaced at $l = 0.12$ mm, and each of them consists of small discrete discharge micronuclei.

Figure 5b shows the structure of discharge in argon at the atmospheric pressure for a heating laser radiation beam with the same parameters as in the case of Fig. 5a ($\tau = 40$ ns, $E = 70$ J, and $\gamma = 7.5°$). However, large-scale funnel-shaped structures spaced at intervals greater than 1 mm are observed in argon.

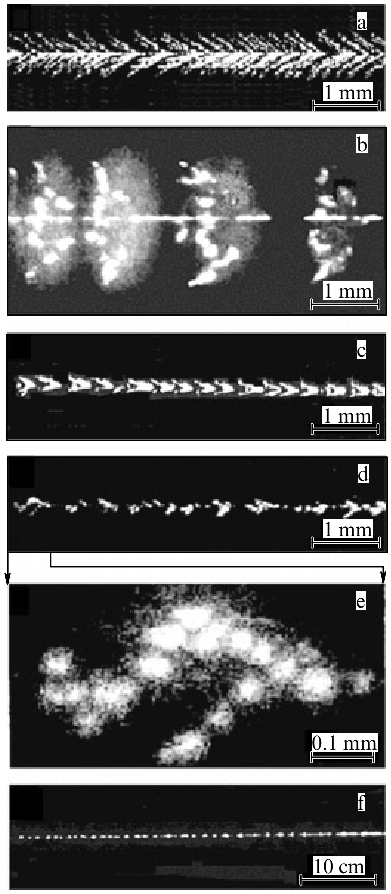

Figure 5. Structures of an optical discharge in Bessel beams: (a) $\tau = 40$ ns, $E = 70$ J, $\gamma = 7.5°$, air at 1 atm; (b) $\tau = 40$ ns, $E = 70$ J, $\gamma = 7.5°$, argon at 1 atm; (c) $\tau = 20$ ns, $E = 20$ J, $\gamma = 5°$, air at 1 atm; (d) $\tau = 0.8$ ns, $E = 17$ J, $\gamma = 2.5°$, air at 1 atm; (e) detail of the photo in Fig. 5d; (f) $\tau = 0.8$ ns, $E = 10$ J, $\gamma = 1°$, argon at 0.2 atm.

As is well known, the threshold intensity is $I_{\rm th} = 1.5 \times 10^{10}$ W cm^{-2} in argon and $I_{\rm th} = 6.5 \times 10^{10}$ W cm^{-2}, i.e., ~ 4.5 times higher, in air [2–6]. Therefore, the excess over the threshold intensity in argon under the same conditions turns out to be substantially larger, which most likely underlies the structure change in passing from air (Fig. 5a) to argon (Fig. 5b). Nevertheless, in this case, the periodically located discharge nuclei (beads) are also seen on the axis, spaced at the interval $l = 0.12$ mm coinciding with the period of the structure presented in Fig. 5a.

The breakdown images in Fig. 5c were obtained with heating pulses of a shorter duration. In particular, the structure depicted in Fig. 5c was produced by a laser beam with the parameters $\tau = 20$ ns, $E = 20$ J, and $\gamma = 5°$ ($L = 26$ cm) in atmospheric air. In this case, the intensity decreased six-fold and the specific energy twelve-fold in comparison with those for the structure in Fig. 5b. The periodicity of the on-axis discharge structure nevertheless showed up in this case, but its period increased to $l = 0.28$ mm and the structure elements turned into continuous plasma nuclei in the paraxial region.

Figure 5d shows a discharge in air at the atmospheric pressure induced by a beam with the parameters $\tau = 0.8$ ns, $E = 17$ J, and $\gamma = 2.5°$ ($L = 52$ cm). In this case, the intensity is almost three times higher and the specific radiation energy is one order of magnitude lower than for the discharge in

Fig. 5c. The longitudinal structure period was $l = 1.1$ mm. Judging by the picture in Fig. 5d, decreasing the specific energy disrupts the uniformity of the type of structure nuclei, but the distribution period remains invariable in this case. It follows that each nucleus consists of smaller cells measuring 0.02–0.05 mm, which group into lines adjoining the axis. A magnified fragment of this picture is shown in Fig. 5d. It clearly shows both the cells themselves and the way they group into separate lines. The angle of inclination β of these lines to the axis is, as before, much larger than the angle of inclination γ of the wave vector $\mathbf{k}$ of the heating radiation.

The breakdown structure in Fig. 5f was obtained in argon at the pressure 0.2 atm using a beam with the parameters $\tau = 0.8$ ns, $E = 10$ J, and $\gamma = 1°$. In this experiment, the intensity was two orders of magnitude lower than the intensity in the previous experiment. For the channel length $Z = 130$ cm, the picture in Fig. 5f shows a 50 cm long portion of the channel. Closer to the axicon (in the left part of the picture), the beam intensity is only a little higher than the breakdown threshold and is equal to about one fourth of the intensity averaged over the entire length (see Fig. 1). The breakdown nuclei are located on the beam axis and make up a sequence of points with the spatial period $l = 7$ mm.

The beam intensity increases with the distance from the axicon and the breakdowns merge together, tending to form a continuous channel. But the scale of the intensity distribution in the beam is independent of the gas composition, pressure, energy, and duration of the heating pulse; it is related solely to the angle γ at the base of the conical radiation wave front.

In experiments involving Bessel beams at the wavelength $\lambda = 1.06$ μm for short-duration laser pulses, $t = 100$ ps, with the rise time $\tau = 20$ ps, the energy level $E = 0.6$ J underlay the choice of nitrous oxide as the medium with a low breakdown threshold. Furthermore, to increase the intensity in the focal segment of the axicon, a relatively large inclination angle of the vectors $\mathbf{k}$ was taken, $\gamma = 18°$, which corresponds to the diameter $2a = 2.6$ μm of the central caustic of the Bessel beam and the length $L = 1.5$ cm.

These experiments were performed at the facility described in detail in Refs [93–96]. The state of the channel was determined from the optical channel inhomogeneities, which were recorded using a Mach–Zehnder interferometer with laser backlighting at the wavelength 0.53 μm for the probing pulse duration 70 ps [87, 88].

In these experiments, however, the beam intensity approached the level of 5×10^{13} W cm^{-2}, at which the absorption of the heating radiation and the development of parametric instabilities begin to affect the field structure [38]. To avoid errors in the interpretation of the effects observed, the temporal progress of the optical discharge was investigated at different pressures. The interferograms are exemplified in Fig. 6. The contours of spark channels stand out against the background of interference fringes of equal inclination. Their local shifts are reflective of the variations of the optical density of the medium.

The interferograms shown in Fig. 6 were recorded with 0, 100, and 250 ps delays of diagnostic backlighting pulses relative to the onset of the heating pulses, at the nitrous oxide pressures 200 Torr (0.27 atm) (Figs 6a–6c) and 500 Torr (0.67 atm) (Figs 6d–6f). Array pixels measuring 1.6 μm are indicated on the interferogram axes. The interferograms in Figs 6a–6c show that the optical discharge channel at the pressure 0.27 atm remains uniform throughout the observation time. On the other hand, we see from the interferograms in Figs 6d–6f that at a higher pressure, 0.67 atm, the interferometer records inhomogeneities during the course of the heating pulse, since the channel inception (for a nearly zero delay of the backlighting).

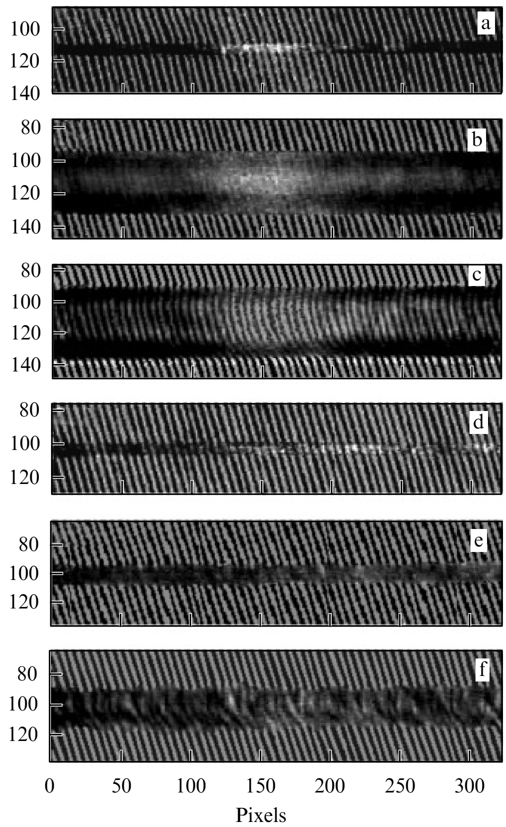

Figure 6. Optical discharge in nitrous oxide for $\tau = 0.1$ ns, $E = 0.6$ J, $\gamma = 18°$: (a–c) $P = 0.27$ atm, with the respective backlighting delays 0, 100, and 250 ps; (d–f) $P = 0.67$atm, with the respective backlighting delays 0, 100, and 250 ps.

The primary discharge nuclei are indiscernible in the interferograms in Figs 6d–6f because of the insufficient spatial resolution of the technique. The general character of fringe shifts in the channel testifies to a discrete structure of the discharge at its inception. Hence, it is believed that primary breakdown nuclei are the source of perturbation waves in the channel. Then, by invoking the technique described in Ref. [97], it is possible to reproduce the spatio-temporal parameters of primary breakdowns from the structure of the perturbation waves and to subsequently gain an insight into the discharge mechanism.

6. Mechanism of optical discharge in a Bessel beam

Along with other discharge characteristics, the mechanisms of the emergence of primary breakdown nuclei in space and time, i.e., coordinates $\mathbf{r}_p$ and the sequence of inception t_p of individual nuclei, their dimensions a and the distribution $f(r \leqslant a)$ of the hydrodynamic parameters in each of them, are interesting. The picture of the perturbation waves produced by primary microbreakdowns forms in the course of propagation of these waves. When the microbreakdown parameters are known, finding the perturbation distribution is a direct problem that is easy to solve. Reconstructing the

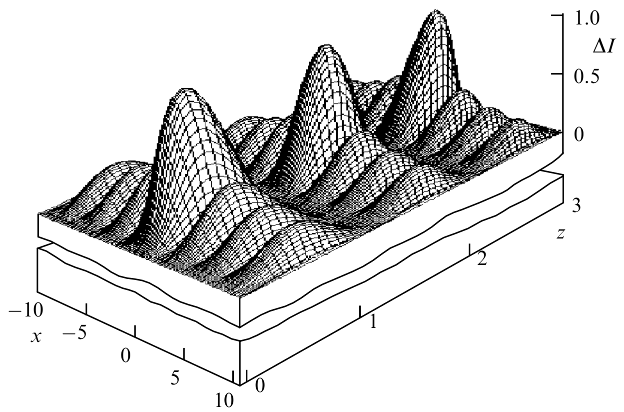

Figure 7. Plot of the Bessel beam structure for $\gamma = 5°$.

primary nuclei parameters from the perturbation distribution is an inverse problem.

As shown in Ref. [38], when the radiation field intensity in the annular zones of the radial distribution becomes close to its self-focusing critical value E_*^2, a longitudinal spatial modulation emerges in the distribution $|E^{(0)}(r,z)|^2$, with the scale given by

$$l = \frac{2\lambda}{\sin^2\gamma}\,. \tag{55}$$

The magnitude of $|E^{(0)}(r,z)|^2$ is then bounded, for instance, in the case of cubic nonlinearity:

$$0.2 \leqslant \frac{n}{n_{\rm cr} - n}\,\frac{1}{\sin^2\gamma}\,\frac{|E^{(0)}|^2}{E_*^2} \leqslant 1\,. \tag{56}$$

The combination of longitudinal (55) and radial (9) field distributions in a Bessel beam makes up a system of longitudinal–annular intensity peaks; a fragment of this structure is depicted in Fig. 7, where the beam radius is represented by the argument of the Bessel function $x = kr\sin\gamma$ and the beam length is expressed in terms of the scale l in (55) of the longitudinal structure, z/l. The value $x = 0$ corresponds to the beam symmetry axis. The distance δr between the neighboring radial peaks is $\delta r \approx \lambda/2\sin\gamma$. Under the conditions of the experiment in Fig. 6f, the scale length of the longitudinal structure is $l = 21$ μm. The radial beam structure is defined by the rings of the Bessel function peaks; on the scale of the channel radius $R = 20.5$ μm, their radii are specified by the following sequence of dimensionless quantities: $a = 0.063, 0.145, 0.227, \ldots$.

When the pulse duration exceeds the characteristic channel expansion time a/c, a discharge emerges at the peaks of beam intensity, and when solution (55) holds, a chain of microbreakdowns emerges on the axis. Each of them produces a local perturbation p of the pressure P with some characteristic diameter $2a$. At a distance $r \gg a$, the perturbation propagates through space as a spherically shaped acoustic wave packet of the thickness $2a$. We represent the pressure variation by an arbitrary function $p \sim f(r)$ to obtain the pressure perturbation [53]

$$\begin{aligned} &\rho = 0\,, && r - a > ct > r + a\,, \\ &\rho \sim f(r)\,\frac{r - ct}{r}\,, && r - a < ct < r + a\,. \end{aligned} \tag{57}$$

Relations (57) describe the propagation of a spherically shaped acoustic wave layer and its internal structure. But it remains unknown how many radial peaks the quantity a comprises and what the time sequence of the breakdowns is, i.e., what the distributions of the breakdowns in space $\mathbf{r}_p$ and in time t_p are.

To answer these questions, we invoke the method for determining pulsations in a tube outlined in Ref. [97]. In doing this, we bear in mind that in the present version of the problem, the primary perturbations emerge near the symmetry axis of the plasma channel rather than at the flow boundary (the tube wall). Let the breakdown regions be confined by one of the Bessel function rings of diameter $2a$, located at the longitudinal maxima. A 512 μm long CCD array accommodates 24 maxima.

Owing to the symmetry of the problem, the wave propagation can be described by two coordinates: the longitudinal coordinate z and the radial one r. To compare the calculation data with the measurement data, the z coordinate and interference fringe shifts are expressed in the scale of h (the interference fringe pitch along the z axis). The structure of perturbations is investigated on the same segment $\{z_1, z_2\} = \{0.55\}$ that was observed in the experiment depicted in Fig. 6f.

The interference fringe shifts in the cylindrical channel correspond to the total phase increment for the probe radiation wave taken along the chord y with an impact parameter r_0. For definiteness, we specify the chord position by the coordinates $r_0 = R/2$ and $z_0 = (z_2 - z_1)/2$. Let the y coordinate vary from 0 to $r_0\tan\varphi$ through half the chord, where φ is the azimuthal angle. The sum of the perturbations at each point of the chord should comprise the action of all waves originating at points z_p along the length of the selected segment $\{z_1, z_2\}$.

Not restricting ourselves to any assumptions, we introduce the following parameters to describe the perturbations: the possible shift Q of the sequence of points z_p as a whole, $Q < 1$; the interval q of random deviations of the points z_p from their uniform distribution, $q < 0.5$; the duration t_0 of that part of the heating pulse τ in which a breakdown occurs; the interval t_p of the random spread of the breakdown instant at the points z_p, $t_p \leqslant t_0$; the number k of microbreakdowns along the length $\{z_1, z_2\}$ with the inclusion of edge effects; the density distribution $f(r < a)$ in a primary microbreakdown; and the number m of summation elements along half the chord y.

We express the quantities t_p, t_o, and τ in the scale of the time of channel development prior to the instant of structure observation, 250 ps, such that the heating pulse duration is $\tau = 0.4$. We write the complete version of the initial conditions of the problem:

$$\begin{aligned} &a = \{0.063,\ 0.145,\ 0.227\}\,, \quad k = 25\,, \quad \tau = 0.4\,, \quad t_0 = 0.4\,, \\ &\{z_1, z_2\} = \{-1, 56\}\,, \quad \{y_1, y_2\} = \left\{0,\ r_0\tan\frac{\pi}{3}\right\}, \\ &f(r) = 1\,, \quad m = 11\,, \quad Q = 1\,, \quad q = 0\,. \end{aligned} \tag{58}$$

Figure 8 shows the calculated and measured data for initial perturbations whose scales are defined by the dimensionless radii $a = 0.063, 0.145$, and 0.227 (the central part and the first and second rings of the Bessel function). The left column shows the density distributions along the line $r_0/R = 0.5$ and the right column gives the spatial spectra of

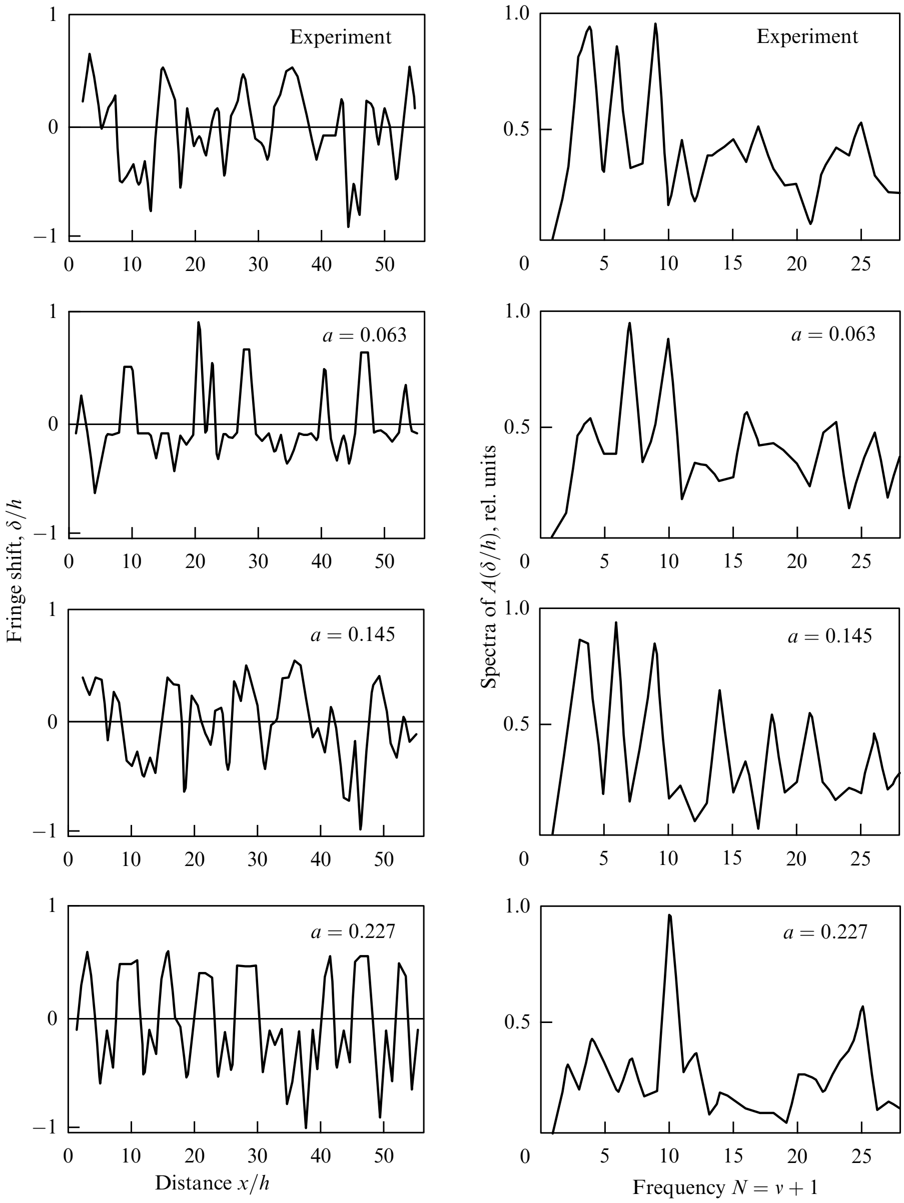

Figure 8. Structure of pulsations along the line $r_0/R = 0.5$ according to experimental and calculated data for $a = 0.063$, 0.145, and 0.227.

these distributions. A comparison of the distributions and spectra in Fig. 8 suggests that the plots for the relative value $a = 0.145$ exhibit the best agreement with experiment. For $a = 0.063$, the structure scale turns out to be too small in comparison with the measurement data. For $a = 0.227$, by contrast, the scale is too large.

The further refinement of primary perturbation parameters was therefore made for the value $a = 0.145$. Variations were made of the number k of perturbations, their distribution along the z_p axis, the displacement Q of the entire perturbation sequence, the range q of possible individual perturbation deviations from the periodic distribution, the period t_0 of breakdown initiation, and the form of the function $f(r)$.

It turned out that the best agreement between the calculated dependences and the experimental data was reached for the following values of the fitting parameters:

$$k = 25\,, \quad t_0 = 0.2\,, \quad Q = 0.17\,, \quad q = 0\,, \quad f(r) = 1\,. \quad (59)$$

According to these results, microbreakdowns in the beam emerge during the time $t_0 = 0.2$ (50 ps) at each axial peak and deviations from the period $l = 21$ μm do not exceed several percent. The dimension of a primary breakdown does not go beyond the second zero of the Bessel function, which corresponds to the radius 2.9 μm. Within the time $t_0 = 0.2$ (50 ps), the breakdown of the medium occurs for a radiation intensity at the level of 0.8 of its peak, while the intensity turns out to be insufficiently high to induce a breakdown in the third and next annular peaks of the Bessel function.

Therefore, for the heating pulse energy $E = 0.6$ J and the duration $\tau = 100$ ps, the optical discharge structure is underlain by the mechanism of nonlinear interaction between the heating radiation and the resultant plasma. According to this mechanism, primary breakdowns of the longitudinal optical discharge structure emerge at the peaks of the Bessel function, including those rings for which the intensity satisfies condition (56).

In the course of the heating pulse, $t_0 = 50$ ps, the boundary of an elementary breakdown shifted by no more

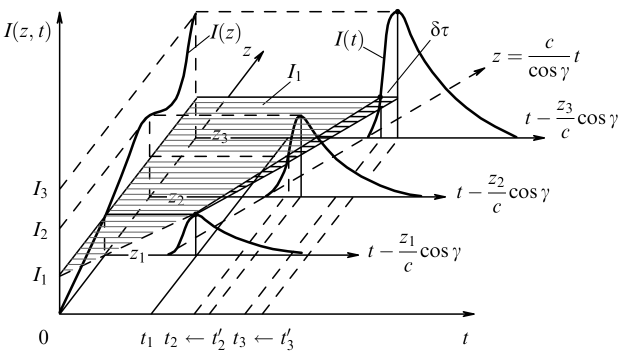

Figure 9. Schematic of beam propagation along the beam axis.

than 1 μm, and the microbreakdown itself was a point-like explosion with a freely moving explosion wave. The established mechanism allows describing all the kinds of optical discharge structures depicted in Fig. 5, bearing in mind the effect of the heating pulse lengthening on the microbreakdown development.

A wealth of data on the propagation of an optical discharge has been accumulated in the investigation of a laser spark in the focus of a spherical lens. According to Refs [2–7], the breakdown threshold is proportional to the ionization potential and decreases with increasing the pressure, the diameter of the focal volume, and the duration of the heating pulse. The breakdown zone moves in opposition to the laser radiation in accordance with one of the mechanisms such as the ionization wave, breakdown wave, or laser-supported detonation with a speed of the order of 10^7 cm s^{-1} or even higher. The optical discharge develops asymmetrically, because only a thermal plasma expansion occurs in other directions, which propagates with a substantially lower speed, $10^6 - 5 \times 10^6$ cm s^{-1}.

Similar effects should occur in the focusing of radiation by an axicon. However, in this case, the breakdown is also affected by the structure of the Bessel beam field and the breakdown propagation in the moving focus regime. The propagation of the nonlinear interaction front along the beam axis is schematized in Fig. 9. The intensity modulus distribution along the axis is represented by the function $I(z, t)$; temporal variation of the heating radiation intensity is given for on-axis points z_1, z_2, and z_3. The dashed surface denotes the lower intensity level I_1 whereby nonlinear processes manifest themselves in accordance with conditions (56).

Below this level, for $I < I_1$, the beam intensity increases monotonically along the axis. For $I > I_1$, a longitudinal intensity modulation occurs with peaks at z_2 and z_3, which is depicted by the bold line $I(z)$ in the vertical plane $z{-}I$. This accounts for the enhancement of microbreakdowns with an increase in the z coordinate and their tendency to merge. At the points z_1, z_2, and z_3, the intensity reaches its peak at the respective instants t_1, t_2', and t_3'. The interaction nonlinearity manifests itself only at the points z_2 and z_3, the onset of breakdown occurring at the instants t_2 and t_3 even prior to the occurrence of intensity peaks at these instants.

Therefore, the breakdown occurs sequentially at points z_{n-1} and z_n if the pulse field attains the breakdown magnitude earlier than the front of the wave travels the distance $z_n - z_{n-1}$, i.e., if $\Delta\tau < (z_n - z_{n-1})/V$. Refining condition (31), we write

$$\Delta\tau < \frac{l\cos\gamma}{c}\,. \tag{60}$$

For a longer pulse duration, the sequence of breakdowns may be violated.

The radial distribution of discharge exhibits special features of its own. When the intensity just begins to exceed the threshold value, the breakdown occurs only in the central caustic, $x_0 = 2.4$. As the energy of the laser pulse increases, the primary breakdown zone covers new, increasingly distant off-axis rings of the Bessel function. As the microbreakdown diameter increases, the distance in which the wave field affects the channel structure also increases (at a ratio a_i/a_0). This effect shows up in a decrease in the ionization potential and accordingly in a change of the bounds in (56) for the neighboring radial peaks. That is why lengthening the pulse changes the character and direction of discharge propagation.

In estimating this direction β, we note that primary breakdown nuclei emerge most likely in the region of localization of the central caustic and the first rings of the radial beam structure. But in a Bessel beam, unlike in spherical focusing, other intensity peaks exist outside the breakdown region. The beam field is capable of maintaining the propagation of an optical discharge in each of these peaks. When a peak falls within the domain of propagation of an ionization wave, which decreases the electric strength of the medium, a new breakdown nucleus accordingly forms in the medium and defines the breakdown propagation direction β. A peculiar interplay of the radiative (ionization) mechanism and the breakdown wave mechanism occurs.

Let **v** and **u** be the velocities of propagation in opposition to the beam and in the lateral direction, δr_1 the distance between the neighboring rings of the radial structure, δr_γ the distance between the same rings in the direction of the angle γ, and $\delta r_\gamma = \delta r_1/\sin\gamma$. Because $\delta r_\gamma \gg \delta r_1$, the front of lateral plasma expansion travels through the peak of the neighboring ring earlier than the wave moving in opposition to the beam. The axial (along the z axis) and radial wave components can be represented as $vz = v\cos\gamma$ and $v_r = v\sin\gamma + u$. Then the angle β is found from the relation

$$\tan\beta = \frac{v\sin\gamma + u}{v\cos\gamma}\,. \tag{61}$$

Formula (61) permits estimating the u/v ratio from the experimentally measured β angle. For instance, the lobes in Fig. 5a make the angle $\beta = 36°$, and hence $u/v = 0.56$. With an increase in specific power, the intensity greatly exceeds its threshold value and the breakdown spreads over a progressively larger number of rings of the radial structure. The picture of discharge in Fig. 5b clearly testifies to a change in the breakdown mechanism. Here, $\beta = 45°$ and $u/v = 1$, which attests to the detonation mechanism of breakdown nucleus propagation and the transformation of the optical discharge structure in the Bessel wave beam to a system of breakdown groups.

The large dimensions of the nuclei and the high density of plasma electrons largely screen the internal region of the beam from the action of radiation. The intensity at the channel center is sufficient for a breakdown in the axial caustic, but not through the whole length. Therefore, only discontinuous fragments of the side lobes of the structure can

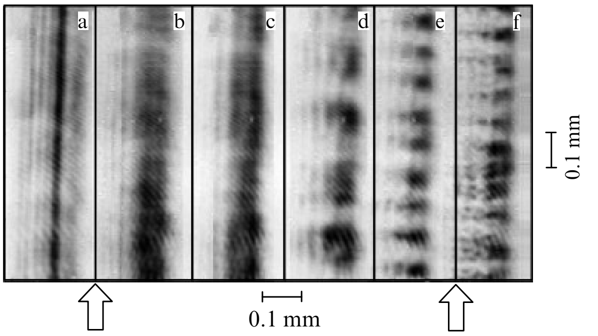

Figure 10. Shadowgrams of the plasma channel at the time instant $t = 330$ ps for the argon pressure (a) 200, (b) 280, (c) 300, (d) 340, (e) 370, and (f) 420 Torr. The heating pulse duration $\tau = 100$ ps, and $I = 5\times10^{13}$ W cm^{-2}.

be seen here. The sparse locations of breakdown groups are also attributable to the screening.

When the heating pulse energy is sufficiently high, the above observations and the picture in Fig. 1b suggest that the structure of the plasma channel in a Bessel beam may be traced only up to the instant of merging of primary breakdown nuclei. After the merging, the channel becomes continuous and virtually uniform. Its further development and the diameter it eventually assumes in the course of its expansion are determined by the specific energy input due to the heating radiation.

A common property of the observed primary breakdown structures is their discreteness, which is defined by relations (55) and (9) or (26) and which is independent of the pressure and sort of gas. A comparison of the pictures in Fig. 6 shows that this property of discharges in Bessel beams persists when the heating pulse duration is of the order of or higher than the characteristic channel expansion time $\tau \sim a/c$ and the intensity does not exceed $\sim 5\times10^{13}$ W cm^{-2}. However, for shorter pulses and higher intensities, the character of the structure may be different.

In the experiments in Ref. [38], a plasma channel approximately 8 mm long was produced with an axicon with the base angle $\alpha = 25°$ ($L \approx 1.5$ mm) in a pulsed argon jet. The jet of a working gas effusing from a narrow square nozzle [93, 98] in a vacuum was matched to the geometry of the Bessel beam. The gas was fed via a pulsed electromagnetic valve from a receiver at a pressure ranging from 15 to 70 atm. Laser radiation pulses ($\lambda = 1.06$ μm) had the halfwidth 100 ps and the peak intensity 5×10^{13} W cm^{-2}. The plasma channel structure was visualized by interferometric or shadowgraphic techniques and recorded with a CCD camera. The channel was probed with a laser pulse at the frequency of a heating radiation harmonic with the duration of several picoseconds.

Figure 10 shows a series of shadowgrams recorded 330 ps after the onset of a heating pulse at an argon pressure ranging from 200 to 420 Torr. The shadowgrams show a 0.8 mm long portion of the channel. At pressures below 300 Torr, the channel appears to be fairly uniform in the axial direction. But already at 340 Torr, an axial modulation can be clearly seen; for higher pressures, the spatial period depends strongly on the pressure. The data derived by a spatial Fourier transform indicate that the period is equal to 0.14 and 0.09 mm for the respective pressures 340 and 370 Torr.

Interferometric measurements show that axial density oscillations amount to no less than 10%. According to the model proposed in Ref. [38], this kind of modulation is due to

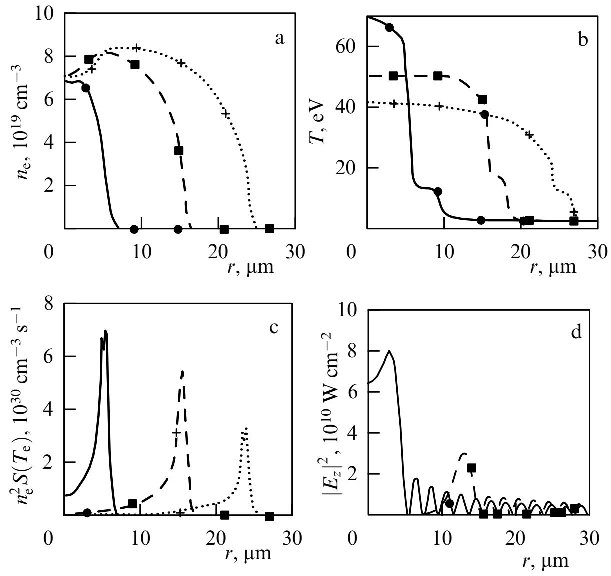

Figure 11. Evolution of plasma channel parameters in argon for the pressure 380 Torr, $\tau = 100$ ps, $I = 5\times10^{13}$ W cm^{-2}: $t = 88$ ps (—●—), $t = 138$ ps (- -■- -), $t = 188$ ps (···●···).

nonlinear absorption, which involves the interaction between the Bessel beam field, the waveguide channel mode, and the axial modulation of plasma channel parameters. With the lapse of time, the beam-induced plasma forms a waveguide whose properties depend on *the profile of the plasma parameters in the channel* and on *the radial and azimuthal order of the relevant mode*.

To determine the plasma parameter profiles during the expansion of the channel produced by a Bessel beam for a short high-intensity heating pulse, the WAKE computer code was used [99–102]. The calculated channel evolution data corresponded to interferometric data in [94, 103, 104]. Figure 11 shows profiles of the electron density n_e, the temperature T_e, and the ionization rate $n^2 S(T_e)$ at three instants of channel development: $t = 88$, 138, and 188 ps. Here, $S = \sum_i S_i(T_e) n_i/n$, where $S_i(T_e) n n_i$ is the collisional ionization rate of an i-fold ionized ion, $S_i(T_e) = 9\times10^{-6}\sqrt{T_e/U_i}\,\exp(-U_i/T_e)/U_i^{3/2}(T_e/U_i + 4.88)$ [105], and U_i is the ionization potential of the ith electron.

For argon, the channel properties were calculated for a 100 ps long pulse of laser radiation ($\lambda = 1.06$ μm) at the intensity 5×10^{13} W cm^{-2}. As is evident from Figs 11a and 11b, the peak of the electron plasma density is located on the channel axis immediately after the breakdown. In this case, collisional heating of the electrons occurs up to the temperature 70 eV and a shock wave is formed. This follows from Fig. 11c, in which the local ionization shows a maximum. By the instant $t = 90$ ps, the electron density peak shifts from the axis in the radial direction. The electron energy subsequently goes to maintain the shock wave, and the channel expansion is attended with a decrease in temperature.

The case exemplified in Fig. 11 corresponds to a relatively high pressure, with the electron density being high enough to affect the distribution of the Bessel beam field. The redistribution of this field is demonstrated by the plot of $|E_z|^2$ in Fig. 11d. At the onset of the heating pulse, the highest intensity of the beam field is concentrated by the axis. But 88 ps later, a partial extrusion of the field from the paraxial region already occurs; and by the instant $t = 138$ ps, the field in the central part of the beam is suppressed almost completely.

In this connection, we consider the *mode structure* of the channel. A Bessel beam can be characterized by the axial wavenumber $k_{\mathrm{a}} = k_0\sqrt{1+4\pi\chi}\cos\gamma$, where $k_0 = \omega_0/c$ is the laser radiation wavenumber and χ is the susceptibility of argon at the pressure $P = 200$ Torr, equal to $\chi = (1/4\pi)1.36\times10^{-4}$. The plasma waveguide has its own wavenumber k_{g}. When the wavenumbers of the beam mode and the waveguide coincide, $k_{\mathrm{a}} = k_{\mathrm{g}}$, linear resonance field absorption occurs [106, 107]. In this case, for some initial gas densities, the beam field produced by the axicon may go beyond the plasma channel at a certain instant to excite a quasiwaveguide mode.

When the channel parameters experience small perturbations with an axial modulation $k_m = k_{\mathrm{g}} - k_{\mathrm{a}} \neq 0$, the beam fields are scattered, giving rise to beats and local plasma heating proportional to the radiation intensity. Modulated heating leads to an exponential enhancement of the small axial modulation k_m of the channel parameters, strengthening the absorption of the Bessel beam field. This type of resonance absorption is nonlinear and occurs due to parametric instability. Because the inclination angle γ of the wave vectors of the heating radiation is usually small, with $\cos\gamma\approx1$, the wavenumber k_m depends only slightly on the angle γ. This feature of the interaction of high-power heating radiation pulses is different from the parametric instability considered above, whereby the plasma channel structure is highly sensitive to the magnitude of the γ angle.

In this model, the electric field of the beam consists of the axicon-produced field E_{a} and the weak scattered radiation field $\tilde{E}_{\mathrm{s}}$:

$$E(r,t) = \mathrm{Re}\left\{E_{\mathrm{a}}(r)\exp\left[\mathrm{i}(k_{\mathrm{a}}z-\omega_0 t)\right] + \tilde{E}_{\mathrm{s}}(r,z,t)\exp\left[\mathrm{i}(k_{\mathrm{s}}z+m\gamma-\omega_0 t)\right]\right\}. \qquad (62)$$

The electron density is the sum of the main symmetric part and a small perturbation related to the modulation:

$$n_{\mathrm{e}}(r,t) = n_0(r) + \mathrm{Re}\left\{\tilde{n}(r,t)\exp\left[\mathrm{i}(k_m z+m\gamma)\right]\right\}. \qquad (63)$$

The amplitude of the radial beam field, which is assumed to be linearly polarized, satisfies the differential equation

$$\left[\nabla_\perp^2 + \kappa^2(r,\omega_0,k_{\mathrm{a}})\right]E_{\mathrm{a}}(r) = 0\,, \qquad (64)$$

where $\kappa^2 = k_0^2(1+4\pi\chi) - k_{\mathrm{a}}^2 - 4\pi r_{\mathrm{e}} n_0(r)(1+\nu/\omega_0)^{-1}$, ν is the electron–ion collision frequency, and r_{e} is the classical electron radius. The electron density profile $n_0(r)$ is determined with the inclusion of ionization, Joule heating, and thermal conduction. The beats of the axicon field and the density modulation excite the scattered wave with the polarization of the incident wave:

$$\left[\nabla_\perp^2 + 2\mathrm{i}\,\frac{\omega_0}{c^2}\frac{\partial}{\partial t} + \kappa^2(r,\omega_0,k_{\mathrm{s}})\right]\tilde{E}_{\mathrm{s}}(r,t) = 4\pi r_{\mathrm{e}} n_{\mathrm{e}0}(r,t)E_{\mathrm{a}}\,. \qquad (65)$$

The complex amplitude of the electron density perturbation, like that of other parameters, is represented in the form $\tilde{n} = \hat{n}\exp(\beta t)$, and the plasma is treated as an ideal gas: $\hat{p} = n_0\hat{T} + \hat{n}T_0$. If the axicon-produced field has the profile $u_{\mathrm{a}}(r) = E_{\mathrm{a}}(r)/E_{\mathrm{a}0}$, the amplitude $E_{\mathrm{a}0}$, and the scattered field profile $u_{\mathrm{s}}(r) = E_{\mathrm{s}}(r)/E_{\mathrm{a}0}$, then the electron density modulation amplitude is given by

$$\frac{\tilde{n}}{n_0} = \frac{c^2}{\omega_{\mathrm{p}}^2\Delta}\left[\nabla_\perp^2\left(\frac{\beta_0^3}{\beta^3}\,u_{\mathrm{s}}u_{\mathrm{a}}^*\right) + \nabla_\perp\left(\frac{\beta_{\mathrm{p}}^2}{\beta^2}\,\nabla_\perp u_{\mathrm{s}}u_{\mathrm{a}}^*\right) + \frac{\omega_{\mathrm{p}}^2}{c^2}\left(\frac{\beta_{\mathrm{I}}^2}{\beta^2}+\frac{\beta_{\mathrm{s}}^2}{\beta^2}\right)u_{\mathrm{s}}u_{\mathrm{a}}^*\right]. \qquad (66)$$

Equation (66) is a consequence of linearized conservation equations [38]. Here, $\Delta = 1 + \nu_{\mathrm{I}}(\eta-2)/\beta$, $\nu_{\mathrm{I}} = n_0 S$ is the radial change of the ionization rate, and $\eta = \mathrm{d}\ln S/\mathrm{d}\ln T_{\mathrm{e}}$. The parameters

$$\beta_0^3 = \frac{2}{3}\,k_{\mathrm{p}}^2\,\frac{m_{\mathrm{e}}}{m_{\mathrm{i}}}\,\nu V_{\mathrm{osc}}^2\,,\quad \beta_{\mathrm{p}}^2 = \frac{\beta_0^3}{3\nu}\,,\quad \beta_{\mathrm{I}}^2 = \frac{2}{3}\,\nu_{\mathrm{I}}\eta\,\frac{m_{\mathrm{e}}}{T_{\mathrm{e}}}\,\nu V_{\mathrm{osc}}^2\,,$$

$$\beta_{\mathrm{s}} = \frac{\nu_{\mathrm{I}}\eta V_{\mathrm{osc}}^2}{\omega^2 r_n r_T}\,,\qquad V_{\mathrm{osc}}^2 = \left(\frac{e}{m_{\mathrm{e}}}\right)^2\frac{|E_{\mathrm{a}0}|^2}{\omega_0^2+\nu^2}$$

are the growth rates of the corresponding quantities and the electron oscillation rate in the axicon and scattering fields. The parameter $r_{n,T}^{-1} = \mathrm{d}\log(n,T)/\mathrm{d}r$ is the inverse of the density and temperature scales.

Equations (63) and (64) lead to a differential equation for the profile of the scattered field $\hat{u}_{\mathrm{s}}(r)$ and its growth rate $u_{\mathrm{s}}(\mathbf{r}) = \hat{u}_{\mathrm{s}}(r)\exp(\mathrm{i}m\beta)$ for the eigenvalues of the growth rate $\beta(k_{\mathrm{s}},t)$, which can be written as the second-order differential equation

$$M(r)\,\frac{\mathrm{d}^2}{\mathrm{d}r^2}\,\hat{u}_{\mathrm{s}}(r) + N(r)\,\frac{\mathrm{d}}{\mathrm{d}r}\,\hat{u}_{\mathrm{s}}(r) + Q(r)\hat{u}_{\mathrm{s}}(r) = 0 \qquad (67)$$

with the coefficients

$$M(r) = 1 + \nu_{\mathrm{I}}\,\frac{\eta-2}{\beta} - \frac{\omega_0|u_{\mathrm{a}}(r)|^2}{2(\omega_0+\mathrm{i}\nu)}\left(\frac{\beta_0^3}{\beta^3}+\frac{\beta_{\mathrm{p}}^2}{\beta^2}\right), \qquad (68)$$

$$N(r) = 1 + \nu_{\mathrm{I}}\,\frac{\eta-2}{\beta} - \frac{\omega_0 u_{\mathrm{a}}(r)}{2(\omega_0+\mathrm{i}\nu)}\left[\frac{r\,\mathrm{d}}{\mathrm{d}r}\left(\frac{\beta_0^3}{\beta^3}\,u_{\mathrm{a}}^*\right) + \frac{\mathrm{d}}{\mathrm{d}r}\left(\frac{r\beta_0^3}{\beta^3}\,u_{\mathrm{a}}^*\right) + \frac{\mathrm{d}}{\mathrm{d}r}\left(\frac{r\beta_{\mathrm{p}}^2}{\beta^2}\,u_{\mathrm{a}}^*\right) + \frac{r\beta_{\mathrm{p}}^2}{\beta^2}\,\frac{\mathrm{d}u_{\mathrm{a}}^*}{\mathrm{d}r}\right], \qquad (69)$$

$$Q(r) = \left(1+\nu_{\mathrm{I}}\,\frac{2-\eta}{\beta}\right)\left(\kappa^2-\frac{m^2}{r^2}\right) + \frac{\omega_0|u_{\mathrm{a}}(r)|^2}{2(\omega_0+\mathrm{i}\nu)}\,\frac{\omega_{\mathrm{p}}^2}{c^2}\,\frac{\beta_{\mathrm{I}}^2}{\beta^2} - \frac{\omega_0 u_{\mathrm{a}}(r)}{2(\omega_0+\mathrm{i}\nu)}\left[\frac{\mathrm{d}}{r\,\mathrm{d}r}\,\frac{r\,\mathrm{d}}{\mathrm{d}r}\left(\frac{r\beta_0^3}{\beta^3}\,u_{\mathrm{a}}^*\right) - \frac{m^2}{r^2}\left(\frac{\beta_0^3}{\beta^3}\,u_{\mathrm{a}}^*\right) + \frac{\mathrm{d}}{r\,\mathrm{d}r}\left(\frac{r\beta_{\mathrm{p}}^2}{\beta^2}\,\frac{\mathrm{d}}{\mathrm{d}r}\,u_{\mathrm{a}}^*\right) - \frac{m^2}{r^2}\left(\frac{\beta_{\mathrm{p}}^2}{\beta^2}\,u_{\mathrm{a}}^*\right)\right]. \qquad (70)$$

The eigenvalue of the exponent $\beta(k_{\mathrm{s}},t)$ depends parametrically on the time and the wavenumber k_{s} via ionization, heating, and ponderomotive physics. The growth in perturbations in different modes with different values of the modulation wavenumber $k_m = k_{\mathrm{s}} - k_{\mathrm{a}}$ is defined by the effective quantity $\Gamma(k_{\mathrm{s}}) = \int\mathrm{d}t\,\beta(k_{\mathrm{s}},t)$. Clearly observed in experiments are modulations with the greatest value of $\Gamma(k_{\mathrm{s}})$. The data in Ref. [38] suggest that the modes with parameters from $m=0$ to $m=2$ satisfy these conditions. The variation of the k_m number with pressure, which was obtained experimentally and calculated for fastest-growth modes, is depicted in Fig. 12a. A comparison of the theoretical dependences and

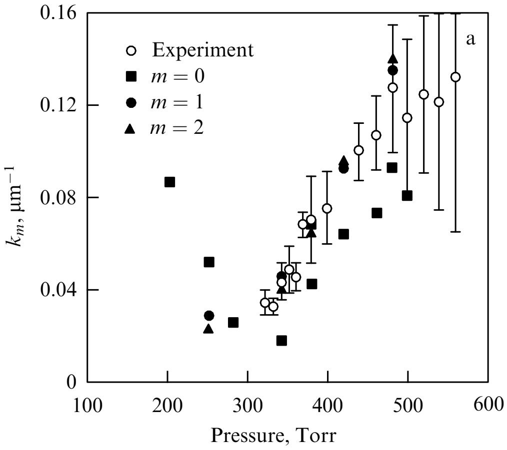

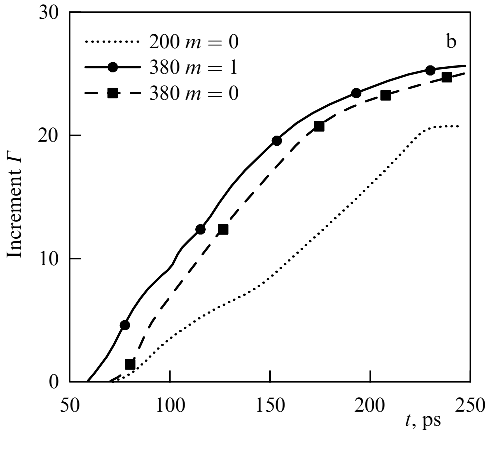

Figure 12. Modulation parameters in the form of the functions $k_m(p)$ and $\Gamma = \int \beta(k_s, t)\,dt$.

the experimental data shows that these results are in close agreement and describe the increase in the wavenumber k_m with pressure quite well.

The correct theoretical description of the process parameters permits estimating the mode instability increments $\Gamma = \int \gamma(k_s, t)\,dt$ during the course of a pulse. These dependences are shown in Fig. 12b for fastest-development modes at pressures 200 and 380 Torr. At the pressure 380 Torr, the $m = 1$ mode has an advantage: we can see from the plot that the quantity Γ for this mode becomes equal to 20 by the midpoint of the period of the heating pulse action, $t = 150$ ps. At the pressure 200 Torr, this result is reached by the instant of cessation of the heating pulse, $t = 220$ ps, while the heating pulse action at the midpoint of the period is $\Gamma = 8$.

We note that Eqn (65) was obtained without taking the electron thermal conduction in the plasma waveguide into account. However, early in the evolution of the channel, when the electron temperature is high and the channel diameter is small, it may play an important role by affecting the field distribution $|E_s(r)|^2$ and Eqn (67). While the instability for a low thermal conductivity is caused primarily by Joule heating and ionization, the contribution due to the ponderomotive force now becomes significant. That is why the overall effect of including the thermal conductivity reduces to the suppression of the $m > 0$ modes and the prevalence of the $m = 0$ modes. It is assumed that the true solution lies somewhere between these extreme cases. Equation (67) with the electron thermal conduction taken into account, its solution, and a detailed comparison of the results are discussed in Ref. [38].

7. Conclusion

We have discussed the processes responsible for the emergence of plasma channels in the caustic of an axicon. A distinguishing feature of these channels is that the optical discharge occurs in the Bessel beam $J_n(r)$ to form an extended plasma waveguide with a diffraction-limited diameter and a large value of the Rayleigh length parameter, $Z_R = \pi d^2/\lambda \gg 1$. For a short rise time of the heating pulse, the breakdown wave propagates along the beam axis in the mode of a moving focus at a speed exceeding the speed of light. The plasma channel expansion corresponds approximately to the theory of a strong cylindrical explosion and depends on the energy input.

The longitudinal and transverse profiles of plasma channel parameters depend on the intensity distribution over the transverse section of the Bessel beam, which may be configured differently. In particular, the intensity may be tubular in shape, of the type J_n^2 $(n > 0)$. The capability to vary the distribution of parameters and control the channel structure is important for applications. In this respect, the cylindrical channel symmetry offers additional advantages in comparison with the spherical one because it allows the effective use of a magnetic field in various applications, for instance, for magnetic plasma confinement.

In the application of the Bessel beam considered in this review, the discharge was generated in gases in the field of laser radiation. However, a transparent liquid and a solid may also fulfill the function of the medium under irradiation. Furthermore, to produce Bessel beams, the electromagnetic radiation of other ranges as well as wave radiation of a different nature, for instance, acoustic, can be used [108].

Acknowledgments
This work was supported by the Russian Foundation for Basic Research (Grant No. 05-08-50238-a).

References

1. Maker H D, Terhune R W, Savage C M, in *Quantum Electronics: Proc. of the 3rd Intern. Congress, Paris, France, 1963* (Eds P Grivet, N Bloembergen) (Paris: Dunod; New York: Columbia Univ. Press, 1964) p. 1559
2. Raizer Yu P *Usp. Fiz. Nauk* **87** 29 (1965) [*Sov. Phys. Usp.* **8** 650 (1966)]
3. Raizer Yu P *Lazernaya Iskra i Rasprostranenie Razryadov* (Laser-Induced Discharge Phenomena) (Moscow: Nauka, 1974) [Translated into English (New York: Consultants Bureau, 1977)]
4. Raizer Yu P *Usp. Fiz. Nauk* **132** 549 (1980) [*Sov. Phys. Usp.* **23** 789 (1980)]
5. Raizer Yu P *Osnovy Sovremennoi Fiziki Gazorazryadnykh Protsessov* (The Foundations of Modern Gas Discharge Physics) (Moscow: Nauka, 1980)
6. Ostrovskaya G V, Zaidel' A N *Usp. Fiz. Nauk* **111** 579 (1973) [*Sov. Phys. Usp.* **16** 834 (1974)]
7. Raizer Yu P (Ed.) *Deistvie Lazernogo Izlucheniya* (Effects of Laser Radiation) Collection of papers (Moscow: Mir, 1968)
8. Durnin J *J. Opt. Soc. Am. A* **4** 651 (1987)
9. Durnin J, Miceli J J (Jr.), Eberly J H *Phys. Rev. Lett.* **58** 1499 (1987)
10. Zel'dovich B Ya, Pilipetskii N F *Izv. Vyssh. Uchebn. Zaved. Ser. Radiofiz.* **9** (1) 95 (1966) [*Radiophys. Quantum Electron.* **9** 64 (1966)]

11. Zel'dovich B Ya, Mul'chenko B F, Pilipetskii N F *Zh. Eksp. Teor. Fiz.* **58** 793 (1970) [*Sov. Phys. JETP* **31** 425 (1970)]
12. Pyatnitskii L N, Korobkin V V "Volnovye puchki s kompensirovannoi difraktsiei i protyazhennye plazmennye kanaly na ikh osnove" ("Wave beams with compensation for diffraction and extended plasma channels on their basis") *Tr. Inst. Obshch. Fiz. Ross. Akad. Nauk* **57** 59 (2000)
13. Bunkin F V, Korobkin V V, Kurinyi Yu A, Polonskii L Ya, Pyatnitskii L N *Kvantovaya Elektron.* **10** 443 (1983) [*Sov. J. Quantum Electron.* **13** 254 (1983)]
14. Korobkin V V, Polonskii L Ya, Poponin V P, Pyatnitskii L N *Kvantovaya Elektron.* **13** 265 (1986) [*Sov. J. Quantum Electron.* **16** 178 (1986)]
15. Pyatnitskii L N et al. "Ustroistvo dlya formirovaniya lazernoi iskry" ("Device for laser spark formation"), USSR Inventor's Certificate No. 1082292 (1984); *Byull. Izobret.* (39) 189 (1984); see also Rospatent. Federal Institute of Industrial Property. Inventions (Retrospective Database) — RUPAT_OLD, http://www.fips.ru/
16. Pyatnitskii L N et al. "Ustroistvo dlya polucheniya opticheskogo razryada" ("Device for obtaining an optical discharge"), USSR Inventor's Certificate No. 1189322 (1986); *Byull. Izobret.* (12) 282 (1986); see also Rospatent. Federal Institute of Industrial Property. Inventions (Retrospective Database) — RUPAT_OLD, http://www.fips.ru/
17. Pyatnitskii L N et al. "Ustroistvo dlya formirovaniya besselevykh puchkov elektromagnitnogo izlucheniya v odnorodnoi prozrachnoi srede" ("Device for the formation of Bessel beams of electromagnetic radiation in a uniform transparent medium"), USSR Inventor's Certificate No. 1753446 (1992); *Byull. Izobret.* (29) 184 (1992); see also Rospatent. Federal Institute of Industrial Property. Inventions (Retrospective Database) — RUPAT_OLD, http://www.fips.ru/
18. Bychkov S, Marin M, Pyatnitsky L, in *X-ray Lasers 1992: Proc. of the 3rd Intern. Colloquium, Schliersee, Germany, 18 – 22 May 1992* (Ed. E E Fill) (Bristol: IOP Publ., 1992) p. 439
19. Polonskii L Ya, Pyatnitskii L N, Uvaliev M I "Plazmennyi lazer" ("Plasma laser"), USSR Inventor's Certificate No. 1432642 (1988); *Byull. Izobret.* (39) 243 (1988)
20. Bychkov S S, Marin M Yu, Pyatnitskii L N "Nepreryvnaya lazernaya iskra" ("Continuous laser-induced spark"), in *Vzaimodeistvie Lazernogo Izlucheniya Sverkhvysokoi Intensivnosti s Plazmoi* (Interaction of Superhigh-Intensity Radiation with Plasmas) (Trudy Inst. Obshch. Fiz. Ross. Akad. Nauk, Vol. 50) (Moscow: Nauka, 1995) p. 166
21. Korobkin V V, Pil'skii V I, Polonskii L Ya, Pyatnitskii L N "Impul'snyi elektronnyi uskoritel'" ("Pulsed electron accelerator"), USSR Inventor's Certificate No. 1082294; *Byull. Izobret.* (11) (1984)
22. Marin M Yu et al. *Pis'ma Zh. Tekh. Fiz.* **12** 1072 (1986)
23. Polonskiy L Ya, Goltsov A Yu, Morozov A V *Phys. Plasmas* **3** 2781 (1996)
24. Bychkov S S et al. "Kommutatsiya mezhelektrodnogo promezhutka plazmoi besseleva puchka" ("Commutation of an interelectrode gap by the plasma of a Bessel beam"), in *Materialy XIII Mezhdunar. Nauchnoi Shkoly-Seminara po Fizike Impul'snykh Razryadov v Kondensirovannykh Sredakh* (Proc. XIIIth Intern. Scientific School–Workshop on the Physics of Pulsed Discharges in Condensed Media) (Nikolaev, 2007) p. 51
25. Marin M Yu, Pil'skii V I, Polonskii L Ya, Pyatnitskii L N "Razryadnik" ("Switching tube"), USSR Inventor's Certificate No. 1333180; *Byull. Izobret.* (34) 290 (1988); see also Rospatent. Federal Institute of Industrial Property. Inventions (Retrospective Database) — RUPAT_OLD, http://www.fips.ru/
26. Marin M Yu et al. *Pis'ma Zh. Tekh. Fiz.* **10** 1322 (1984) [*Sov. Tech. Phys. Lett.* **10** 558 (1984)]
27. Polonskii L Ya, Pyatnitskii L N, Sheindlin A E "Sposob peredachi elektroenergii" ("A Way of transmitting electric energy"), USSR Inventor's Certificate No. 1152478; *Byull. Izobret.* (12) 184 (1985); see also Rospatent. Federal Institute of Industrial Property. Inventions (Retrospective Database) — RUPAT_OLD, http://www.fips.ru/
28. Marin M Yu, Polonskii L Ya, Pyatnitskii L N *Pis'ma Zh. Tekh. Fiz.* **12** (3) 146 (1986)
29. Polonskii L Ya, Pyatnitskii L N *Opt. Atmos.* **1** (7) 86 (1988)
30. Bystrov A M, Vvedenskii N V, Gildenburg V B *Pis'ma Zh. Eksp. Teor. Fiz.* **82** 852 (2005) [*JETP Lett.* **82** 753 (2005)]
31. Kostin V A, Vvedenskii N V *Czech. J. Phys.* **56** (Suppl. 2) B587 (2006)
32. Gildenburg V B, Vvedenskii N V *Phys. Rev. Lett.* **98** 245002 (2007)
33. Liu C S, Tripathi V K *J. Appl. Phys.* **105** 013313 (2009)
34. Kuzelev M V, Rukhadze A A *Fiz. Plazmy* **27** (2) 170 (2001) [*Plasma Phys. Rep.* **27** 158 (2001)]
35. Vvedenskii N V, Gil'denburg V B *Pis'ma Zh. Eksp. Teor. Fiz.* **76** 440 (2002) [*JETP Lett.* **76** 380 (2002)]
36. Bodrov S B, Gil'denburg V B, Sergeev A M *Zh. Eksp. Teor. Fiz.* **124** 744 (2003) [*JETP* **97** 668 (2003)]
37. Gavrilenko V P et al. *Phys. Rev. A* **73** 013203 (2006)
38. Cooley J H et al. *Phys. Rev. E* **73** 036404 (2006)
39. Polesana P et al. *Phys. Rev. A* **77** 043814 (2008)
40. Akturk S et al. *Opt. Commun.* **282** 129 (2009)
41. Andreev N E et al. *Pis'ma Zh. Tekh. Fiz.* **15** (3) 83 (1989) [*Sov. Tech. Phys. Lett.* **15** 116 (1989)]
42. Andreev N E, Aristov Yu A, Polonskii L Ya, Pyatnitskii L N *Zh. Eksp. Teor. Fiz.* **100** 1756 (1991) [*Sov. Phys. JETP* **73** 969 (1991)]
43. Andreev N E, Aristov Yu A, in *Nonlinear World: IV Intern. Workshop on Nonlinear and Turbulent Processes in Physics, Kiev, 1989* (Eds V G Bar'yakhtar et al.) Vol. 2 (Singapore: World Scientific, 1990) p. 727
44. Marin M Yu, Margolin L Ya, Polonskii L Ya, Pyatnitskii L N *Pis'ma Zh. Tekh. Fiz.* **13** (4) 217 (1987)
45. Marin M Yu et al. *Zh. Tekh. Fiz.* **57** 1507 (1987) [*Sov. Phys. Tech. Phys.* **32** 898 (1987)]
46. Kamushkin A A et al. "Proboi vozdukha odnochastotnym lazernym izlucheniem, sfokusirovannym aksikonom" ("Air breakdown induced by single-frequency laser radiation focused by an axicon") *Kratk. Soobshch. Fiz. FIAN* (11) 40 (1988)
47. Pyatnitsky L N, Polonsky L Ya "Optical breakdown plasma in diffraction-free laser beams", in *XIX Intern. Conf. on Phenomena in Ionized Gases: ICPIG XIX, Invited Lectures. Studio Plus, Belgrade* (1989) p. 342
48. Andreev N E, Margolin L Ya, Pleshanov I V, Pyatnitskii L N *Zh. Eksp. Teor. Fiz.* **105** 1232 (1994) [*JETP* **78** 663 (1994)]
49. Mikhaltsova I A, Nalivaiko V I, Soldatenkov I S *Optik* **67** 267 (1984)
50. Polonskii L Ya, Pyatnitskii L N "Fokusiruyushchie sistemy iz konicheskikh opticheskikh elementov dlya spektrokhimicheskogo lidara" ("Focusing systems of conical optical elements for a spectrochemical lidar"), in Tezisy Dokladov IX Vsesoyuz. Simpoziuma po Lazernomu i Akusticheskomu Zondirovaniyu Atmosfery, Tuapse, 1986 (Abstracts of the IXth All-Union Symp. on Laser and Acoustic Atmospheric Probing, Tuapse, 1986
51. Ivanov O G et al. *Zh. Tekh. Fiz.* **57** 2012 (1987) [*Sov. Phys. Tech. Phys.* **32** 1212 (1987)]
52. Pyatnitskii L N *Energiya* (12) 24 (1997)
53. Landau L D, Lifshitz E M *Gidrodinamika* (Fluid Mechanics) (Moscow: Nauka, 1988) [Translated into English (Oxford: Pergamon Press, 1987)]
54. Zel'dovich Ya B, Raizer Yu P *Fizika Udarnykh Voln i Vysokotemperaturnykh Gidrodinamicheskikh Yavlenii* (Physics of Shock Waves and High-Temperature Hydrodynamic Phenomena) (Moscow: Fizmatgiz, 1963) [Translated into English (New York: Academic Press, 1966 – 1967)]
55. Braginskii S I *Zh. Eksp. Teor. Fiz.* **34** 1548 (1958) [*Sov. Phys. JETP* **7** 1068 (1958)]
56. Sedov L I *Metody Podobiya i Razmernosti v Mekhanike* (Similarity and Dimensional Methods in Mechanics) (Moscow: Nauka, 1987) [Translated into English (Moscow: Mir Publ., 1982)]
57. Korobkin V V et al. *Zh. Eksp. Teor. Fiz.* **53** 116 (1967) [*Sov. Phys. JETP* **26** 79 (1968)]
58. Zamyshlyaev B V et al. *Sostav i Termodinamicheskie Funktsii Plazmy* (Composition and Thermodynamic Functions of Plasma) Reference Book (Moscow: Energoatomizdat, 1984)
59. Kestenboim Kh S, Roslyakov G S, Chudov L A *Tochechnyi Vzryv. Metody Rascheta. Tablitsy* (Point Explosion. Computing Methods. Tables) (Moscow: Nauka, 1974)
60. Grudnitskij V G, Rygalin V N *Zh. Vychisl. Mat. Mat. Fiz.* **23** 413 (1983) [*USSR Comput. Math. Math. Phys.* **23** (2) 102 (1983)]

61. Colombant D G, Goldstein S A, Mosher D *Phys. Rev. Lett.* **45** 1253 (1980)
62. Sukhodrev N K "O vozbuzhdenii spektra v iskrovom razryade" ("On the spectrum excitation in a spark discharge") *Tr. Fiz. Inst. Akad. Nauk SSSR* **15** 123 (1961)
63. Plooster M N *Phys. Fluids* **13** 2665 (1970)
64. Plooster M N *Phys. Fluids* **14** 2111 (1971)
65. Karlov N V et al. *Pis'ma Zh. Eksp. Teor. Fiz.* **14** 214 (1971) [*JETP Lett.* **14** 140 (1971)]
66. Gasilov V A et al. "Raschet razvitiya osesimmetrichnogo teplovogo vzryva v molekulyarnom gaze" ("Calculation of the development of an axially symmetric thermal explosion in a molecular gas"), Preprint No. 5-138 (Moscow: Inst. of High Temperatures, USSR Acad. of Sciences, 1984)
67. Arsen'ev D A, Skvortsov V A, Sorokin G A, in *Voprosy Dielektromagnitnykh Voln* (Dielectromagnetic Wave Problems) (Moscow: Izd. MFTI, 1982) p. 63
68. Gaifulin S A et al., Preprint (Moscow: M V Keldysh Inst. for Applied Mathematics, USSR Acad. of Sciences, 1983)
69. Stricker J, Parker J G *J. Appl. Phys.* **53** 851 (1982)
70. Armstrong R A, Lucht R A, Rawlins W T *Appl. Opt.* **22** 1573 (1983)
71. Baravian G, Codart J, Sultan G *Phys. Rev. A* **25** 1483 (1982)
72. Baravian G, Codart J, Sultan G *Phys. Rev. A* **14** 761 (1976)
73. Moroz P E *Fiz. Plazmy* **5** 1128 (1979)
74. Moroz P E *Zh. Eksp. Teor. Fiz.* **77** 1367 (1979) [*Sov. Phys. JETP* **50** 688 (1979)]
75. Ginzburg V L, Gurevich A V *Usp. Fiz. Nauk* **70** 201 (1960) [*Usp. Fiz. Nauk* **3** 115 (1960)]
76. Biberman L M, Vorob'ev V S, Yakubov I T *Kinetika Neravnovesnoi Nizkotemperaturnoi Plazmy* (Kinetics of Nonequilibrium Low-Temperature Plasmas) (Moscow: Nauka, 1982) [Translated into English (New York: Consultants Bureau, 1987)]
77. Aleksandrov A F, Rukhadze A A *Fizika Sil'notochnykh Elektrorazryadnykh Istochnikov Sveta* (The Physics of High-Current Electric-Discharge Light Sources) (Moscow: Atomizdat, 1976)
78. Markelova L P, Nemchinov I V, Shubadeeva L P *Zh. Prikl. Mekh. Tekh. Fiz.* (2) 54 (1973) [*J. Appl. Mech. Tech. Phys.* **14** 192 (1973)]
79. Korobkin V V et al. "Dinamika sploshnogo opticheskogo razryada v vozdukhe" ("Dynamics of a continuous optical air discharge"), Preprint No. 5-127 (Moscow: Inst. of High Temperatures, USSR Acad. of Sciences, 1984)
80. Andreev N E, Pleshanov I V, Pyatnitskii L N "Formirovanie i nelineinoe rasprostranenie trubchatykh puchkov elektromagnitnogo izlucheniya" ("Production and nonlinear propagation of tubular electromagnetic radiation beams"), in *Tezisy Dokladov VI Vsesoyuz. Konf. po Vzaimodeistviyu Elektromagnitnogo Izlucheniya s Plazmoi, Dushanbe, 1991* (Abstracts of the VIth All-Union Conf. on the Interaction of Electromagnetic Radiation with Plasma, Dushanbe, 1991)
81. Andreev N E et al. *Kvantovaya Electron.* **23** 130 (1996) [*Quantum Electron.* **26** 126 (1996)]
82. Margolin L Ya, Pil'skii V I, Pyatnitskii L N "Usloviya formirovaniya trubchatykh plazmennykh kanalov v lazernoi iskre" ("Conditions for the formation of tubular plasma channels in a laser-induced spark"), in *VIII Konf. po Fizike Gazovogo Razryada* (VIIIth Conf. on Gas-Discharge Physics) Abstracts. Pt. 2 (Ryazan', 1996) p. 27
83. Andreev N E et al. "Modelirovanie protyazhennoi trubchatoi lazernoi iskry pri proboe geliya" ("Simulations of an extended tubular laser-induced spark in the breakdown of helium"), in *VIII Konf. po Fizike Gazovogo Razryada* (VIIIth Conf. on Gas-Discharge Physics) Abstracts. Pt. 2 (Ryazan', 1996) p. 29
84. Bychkov S S et al. "Protyazhennaya lazernaya iskra trubchatoi konfiguratsii: eksperimental'nye issledovaniya i chislennoe modelirovanie" ("Extended laser-induced spark of tubular configuration: experimental research and numerical simulations"), in *Doklady Konf. po Fizike Nizkotemperaturnoi Plazmy* (Proc. Conf. on the Physics of Low Temperature Plasma) Pt. 1 (Petrozavodsk: Petrozavodskii Univ., 1998) p. 349
85. Bychkov S S et al. *Kvantovaya Electron.* **26** 229 (1999) [*Quantum Electron.* **29** 229 (1999)]
86. Bychkov S S et al. "Spektry izlucheniya gazovoi misheni pod vozdeistviem moshchnykh besselevykh puchkov nitevidnoi i trubchatoi konfiguratsii" ("Emission spectra of a gas target irradiated by high-power Bessel beams of filamentary and tubular configurations"), in *Mezhdunar. Konf. "Uravnenie Sostoyaniya Veshchestva"* (XVth Intern. Conf. "Equation of State of Matter") Abstracts, Terskol, 2000, p. 75
87. Pyatnitskii L N *Fiz. Plazmy* **27** 846 (2001) [*Plasma Phys. Rep.* **27** 799 (2001)]
88. Pyatnitsky L N "Structures of extended laser spark", in *Proc. of the 3rd Intern. Workshop on Magneto-Plasma Aerodynamics in Aerospace Applications* (Moscow: Inst. of High Temperatures, USSR Acad. of Sciences, 2001) p. 407
89. Korobkin V V et al. "Fizicheskie svoistva i zakonomernosti razvitiya sploshnykh protyazhennykh lazernykh iskr" ("Physical properties and development mechanisms of continuous extended laser-induced sparks"), Preprint No. 5-179 (Moscow: Inst. of High Temperatures, USSR Acad. of Sciences, 1985)
90. Kobylyanskii A I et al. "Svoistva sploshnykh protyazhennykh lazernykh iskr v gazakh ponizhennogo davleniya" ("Properties of Continuous Extended Laser-Induced Sparks in Low Pressure Gases"), Preprint No. 5-264 (Moscow: Inst. of High Temperatures, USSR Acad. of Sciences, 1985)
91. Korobkin V V et al. *Kvantovaya Electron.* **12** 959 (1985) [*Sov. J. Quantum Electron.* **15** 631 (1985)]
92. Pyatnitskii L N *Prikl. Fiz.* (1) 55 (2003)
93. Milchberg H M, Durfee C G, Lynch J *J. Opt. Soc. Am. B* **12** 731 (1995)
94. Clark T R, Milchberg H M *Phys. Rev. Lett.* **81** 57 (1998)
95. Nikitin S P et al. *Opt. Lett.* **22** 1787 (1997)
96. Fan J et al. *Phys. Rev. E* **62** R7603 (2000)
97. Pyatnitskii L N *Uravnenie Nav'e–Stoksa i Turbulentnye Pul'satsii* (Navier–Stokes Equation and Turbulent Pulsations) (Moscow: Granitsa, 2006); *Turbulence Nature and the Inverse Problem* (Heidelberg: Springer, 2009)
98. Fiedorowicz H et al. *AIP Conf. Proc.* **332** 538 (1994)
99. Mora P, Antonsen T M (Jr.) *Phys. Rev. E* **53** R2068 (1996)
100. Mora P, Antonsen T M (Jr.) *Phys. Plasmas* **4** 217 (1997)
101. Durfee C G (III), Milchberg H M *Phys. Rev. Lett.* **71** 2409 (1993)
102. Durfee C G (III), Lynch J, Milchberg H M *Phys. Rev. E* **51** 2368 (1995)
103. Clark T R, Milchberg H M *Phys. Rev. Lett.* **78** 2373 (1997)
104. Clark T R, Milchberg H M *Phys. Rev. E* **61** 1954 (2000)
105. McWhirter R W P, in *Plasma Diagnostic Techniques* (Eds R H Huddlestone, S L Leonard) (New York: Academic Press, 1965) p. 201
106. Fan J, Parra E, Milchberg H M *Phys. Rev. Lett.* **84** 3085 (2000)
107. Fan J et al. *Phys. Rev. E* **65** 056408 (2002)
108. Pyatnitsky L N *Pis'ma Zh. Tekh. Fiz.* **28** (6) 66 (2002) [*Tech. Phys. Lett.* **28** 246 (2002)]